Department of Physics and Astronomy
Heidelberg University

Bachelor Thesis in Physics
submitted by

Mika Holzem

born in Lüneburg (Germany)

Juni 2023

Free-streaming approach to linearized fluid dynamics in heavy-ion collisions

This Bachelor Thesis has been carried out by Mika Holzem at the
Physikalisches Institut der Universität Heidelberg
under the supervision of
Prof. Dr. Silvia Masciocchi

Abstract

The behavior of the quark-gluon plasma created in a heavy-ion collision can be modeled well with fluid-dynamics. Event-by-event simulations, however, can become computationally very expensive if one aims to reach an arbitrarily high level of precision to compare to the experimental data. Making use of a background-fluctuation splitting approach employing statistically averaged initial conditions and linearized fluid-dynamic equations saves computation time. However, the background field approach with its linear approximation of the Equation of State can become inaccurate in more peripheral collisions, where fluctuations are stronger. It is examined if the range of applicability of the background-fluctuation splitting approach can be widened by introducing a free-streaming pre-equilibrium evolution. To investigate this, the evolution of the fluctuation fields are observed, in order to verify that they decrease as expected with free streaming time. Further, the impact of the free-streamed initial conditions on total energy and total entropy is studied in different centrality classes for different free streaming times. The results for total energy and total entropy are compared with proper event-by-event simulations.
Moreover, a free-streaming+hydro approach is used to investigate the impact on mean particle transverse momentum and mean particle multiplicity in dependence of centrality and free-streaming time.

Zusammenfassung

Das Verhalten des Quark-Gluon-Plasmas, das bei einer Schwerionenkollision entsteht, lässt sich mithilfe von Hydrodynamik gut modellieren. Eine "event-by-event" Simulation kann jedoch sehr rechenintensiv werden, wenn man eine beliebig hohe Genauigkeit im Vergleich zu den experimentellen Daten erreichen will. Die Verwendung eines Ansatzes zur Aufspaltung der Hintergrundfluktuation, unter Verwendung statistisch gemittelter Anfangsbedingungen und linearisierter hydrodynamischer Gleichungen, spart erheblichen Rechenaufwand. Der Ansatz mit seiner linearen Annäherung der Zustandsgleichung kann jedoch bei peripheren Kollisionen, bei denen die Fluktuationen stärker sind, ungenau werden. Es wird untersucht, ob der Anwendungsbereich der Hintergrundfluktuation Aufspaltung durch die Einführung einer "free streaming" Phase, vor dem Einstellen des thermischen Equilibriums, erweitert werden kann. Um dies zu untersuchen, wird die Entwicklung der Fluktuationsfelder beobachtet, um zu überprüfen, ob sie wie erwartet mit der "free streaming" Zeit abnehmen. Außerdem wird untersucht, was die Auswirkungen verschiedener "free streaming" Zeiten auf die Gesamtenergie und die Gesamtentropie der entwickelten Anfangsbedingungen in verschiedenen Zentralitätsklassen ist. Die Werte für Gesamtenergie und Gesamtentropie werden mit denen vergleichen, die man in "event-by-event" Simulationen erhält. Darüber hinaus wird eine "free streaming"- und hydrodynamische Phase kombiniert, um die Auswirkungen auf den mittleren Transversalimpulses und die mittlere Teilchenmultiplizität der Teilchen in Abhängigkeit der Zentralität und der "free streaming" Zeit zu untersuchen.

Contents

1 Introduction

Scales play a fundamental role in physics. If one wants to study the behavior of a system, it is vital to provide the governing scales (energy, length, time, etc.) that are connected to it.

This thesis is written in the scope of high energy physics, where the behavior of matter on very high energy scales is studied. To be more specific, it is about one of the most extreme forms of matter that is known to us so far. It has been found, that with increasing temperature (and therefore energy) matter can not be present in its hadronic form anymore [1]. Instead, there is a new phase, called Quark Gluon Plasma (QGP), where it is expected that quarks and gluons can propagate freely in the system [2]. The existence of QGP was verified for the first time on the 10th February 2000 at CERN [3]. To shed light on this so called "deconfinement" of matter, it is necessary to explain the concept of confinement, which is connected to the Standard Model.

1.1 The Standard Model and deconfinement

The Standard Model forms a theoretical background which describes how matter is formed by elementary particles and how those elementary particles interact with each other.

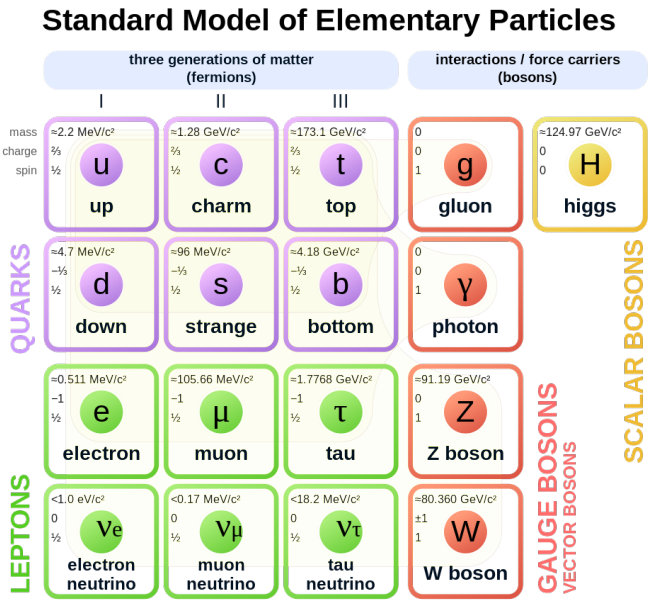

Figure 1: Table of elementary particles included in the Standard Model. In violet the quarks, in green the leptons, in red the gauge bosons and in yellow the Higgs boson. Generations of Fermions are denoted with I, II and III (image adapted from [4])

The model distinguishes 4 groups of particles: The quarks, the leptons, the gauge bosons and the Higgs particle, which is the only scalar boson.
Each particle has a unique ensemble of conserved quantities, such as rest mass, spin, and charges. The gauge bosons are the so-called force carriers and mediate the interaction between the particles. There are three fundamental forces that can be expressed with those particles. The strong interaction is carried by the gluons, the electromagnetic interaction by the photons and the electroweak interaction via the Z and W bosons. Each of those bosons couple to a specific charge. The gluons couple to the color charge, the photons couple to electric charge, and the W and Z boson couple to weak isospin and weak charge.

Typically, it is assumed that there are four fundamental forces, three of which are included in the standard model by the gauge bosons. Gravity however is not part of the standard model and this is one of the reasons the standard model does not qualify as a unified theory, however, it is one of the most accurate theories so far (more information on the standard model e.g., [5]).

It will now be focused on the strong interaction to describe confinement. The only elementary particles which carry color charge are the quarks and the gluon itself. There are three kinds of color charges “red”, “blue” and “green” and their respective anti-color. Quarks are never found free and are always found in bound “color-neutral” states, such as three quark states called the “baryons” with charges red, blue, and green or two quark states called the “mesons” with a color and an anti-color, this is what is called “confinement” [5].
One can picture such systems as a collection of quarks connected via strings [6]. If one now tries to separate those quarks, energy has to be applied to the system in order to stretch the strings.
At some point, the applied energy to the system is so high that a pair-production is possible in which color is conserved, thus resulting in additional bound color-neutral states (see Fig. 2). In this process, no free quark is released. However, with rising temperature, a phase transition occurs where the quarks are liberated due to string condensation [2]. A lot of research is still conducted in order to shed light on the phenomenon of confinement and deconfinement.

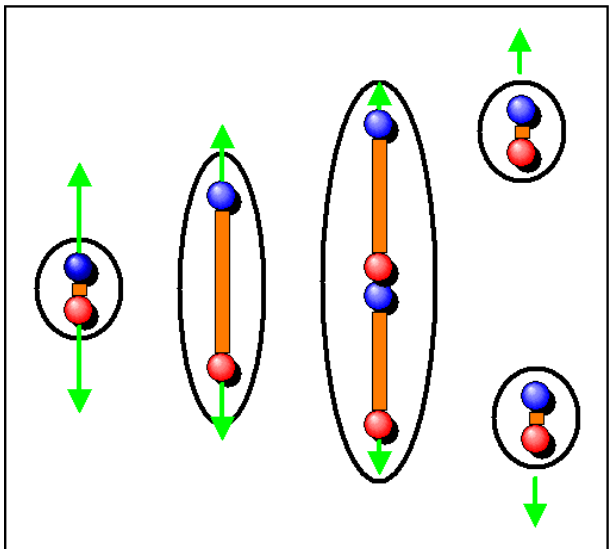

Figure 2: Confinement in the string model shown as example on a meson. In this figure, blue and red describe the color and anti-color (figure adapted from [7])

1.2 Heavy Ion Collisions

To experimentally probe QGP, a tremendous amount of energy density is needed to provide sufficiently high temperatures for it to even form. The critical temperature, over which no hadronic matter can form, is 154MeV [1, 8]. To introduce high energies into a very small volume, the high kinetic energy in particle colliders can be used. Due to their very high mass and thus collision energy, heavy ion collisions are especially suitable.
The LHC (Large Hadron Collider) at CERN is one of the few colliders in the world that can actually realize such conditions. Another hurdle to be overcome is the measurement itself, even though QGP might be produced at a collision point, it can not be directly measured due to its very short lifetime.
What can be measured, are the particles, that are produced in the collision. The measurement of particle species multiplicity (multiplicity refers to the number of particles yielded in a collision) and their momentum can give broad insight in the evolution and properties of QGP. In order to accurately measure the produced particles and their momenta in heavy ion collisions, extremely accurate detectors are used. The experiment at LHC, which is specifically designed for the high multiplicities present in heavy ion collisions, is ALICE (A Large Ion Collider Experiment). In the course of this thesis, data acquired by the ALICE detector at Lead-Lead collision energy of 2.76TeV $\sqrt{s_{NN}}$ (nucleon-nucleon invariant mass) will be used in order to draw comparisons to simulation results.

At collision energies of 2.76TeV $\sqrt{s_{NN}}$, the two ions collide with nearly the speed of

light. A useful measure of velocity not only for the beam, but also for emerging particles, can be introduced by defining rapidity

$$Y = arctanh(\beta_{\parallel}) \tag{1}$$

with $\beta_{\parallel}$ being the velocity in beam direction. This quantity is additive with respect to Lorentz boosts along the beam axis.
At mid-rapidity and at $\sqrt{s_{NN}}$=2.76TeV, one beam would have a rapidity of Y =7.99 When hitting each other, each beam looses about 2 units [9] of rapidity. This means, that they are not stopped completely, but rather fly through each other and during this process deposit a lot of energy in the collision-point of the detector.

Formation and evolution of the QGP

Right after impact, the excited volume needs time to equilibrate, or to thermalize, which means that after a proper time τ the system switches from a deconfined non-thermalized state into one with local thermal equilibrium. The thermalized matter can be described via hydro dynamics as a plasma with deconfined quarks and gluons. The thermalization is expected to occur in a time $\tau \leq$1fm [10].

After thermalization, the system evolves in the form of the QGP and expands until it falls bellow the critical temperature T_c and freezes out. This process, where the quarks and gluons recombine to form hadronic states, is called "Hadronization". The newly produced hadron resonances interact with each other via strong elastic and inelastic collisions.

After further expansion of the hadron resonance gas, the inelastic interactions cease and the abundance of particle species (particle resonances) is fixed. This is called the "chemical freeze-out" and happens at a temperature T_{ch}, which is close to the critical temperature T_c [1].

At even lower temperature after expansion, the hadron gas becomes so sparse, that also the elastic interactions stop. This temperature is called the kinetic freeze-out T_{kin}. At this point on, the momentum distribution of the particles are fixed. Subsequently, the particles fly outward and are measured by the detector.

1.3 Describing experimental data with models

For every collision, that is recorded by the experiment, the number of charged particles and their momenta are determined. However, the collisions differ in their overall charged particle yield and can be divided into groups of similar charged particle yields called centrality classes. The centrality classes are usually defined in percent (see Fig. 3). Thus, 0-5% defines for example the most central collisions. In those centrality classes, one can determine the mean values of particle species multiplicity or particle species momentum, which are suited for the comparison to simulated data.

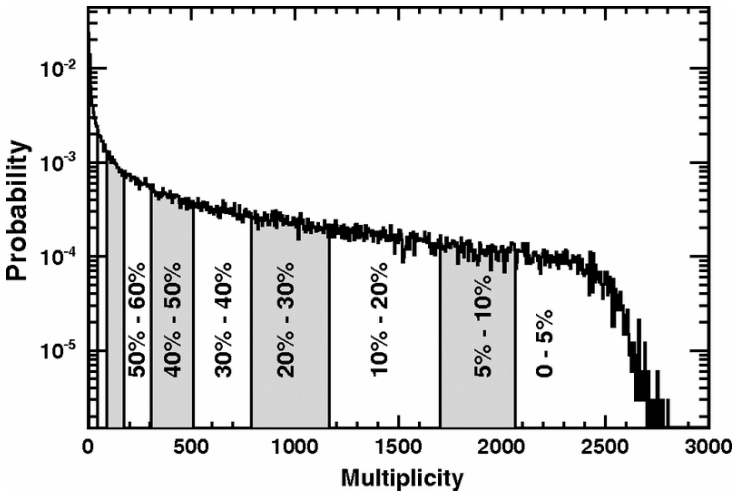

Figure 3: Probability to charged particle multiplicity recorded in the TPC (Time Projection Chamber) of ALICE (figure from [11])

When developing a model for heavy ion collisions, one can mimic the phases described before in section 1.2. An impact model will simulate the collision of the two nuclei, and the deposition of energy. There are initial condition models, which provide a simulation in 3 dimensions, but also initial condition models, which simulate 2-dimensional fields. Further, not only energy deposition, but also momentum distribution can be provided by some models. A very simple model, which still gives a good prediction of data, is the Glauber model [12]

The pre-equilibrium is sometimes simulated using dynamical initial condition models, such as the IP-Glasma model [13]. In some cases, the pre-equilibrium is neglected due to the short time of influence it has on the dynamics of the system ($\tau \leq$1fm). However, it has been shown that pre-equilibrium effects can exert a non-negligible influence on subsequent dynamics [14].

The state of the system after thermalization is then further evolved using a hydrodynamic model until the fluid reaches the critical temperature. The hadronization is carried out

using the hadronization model, which in some cases implements the dynamics of the soft and hard scattering of the hadron resonance gas. The simulation is carried out event-by-event and is subsequently sorted into centrality classes. The results for observables from these classes can be compared to experimental results. A graphical representation of the procedure can be seen in Fig. 4

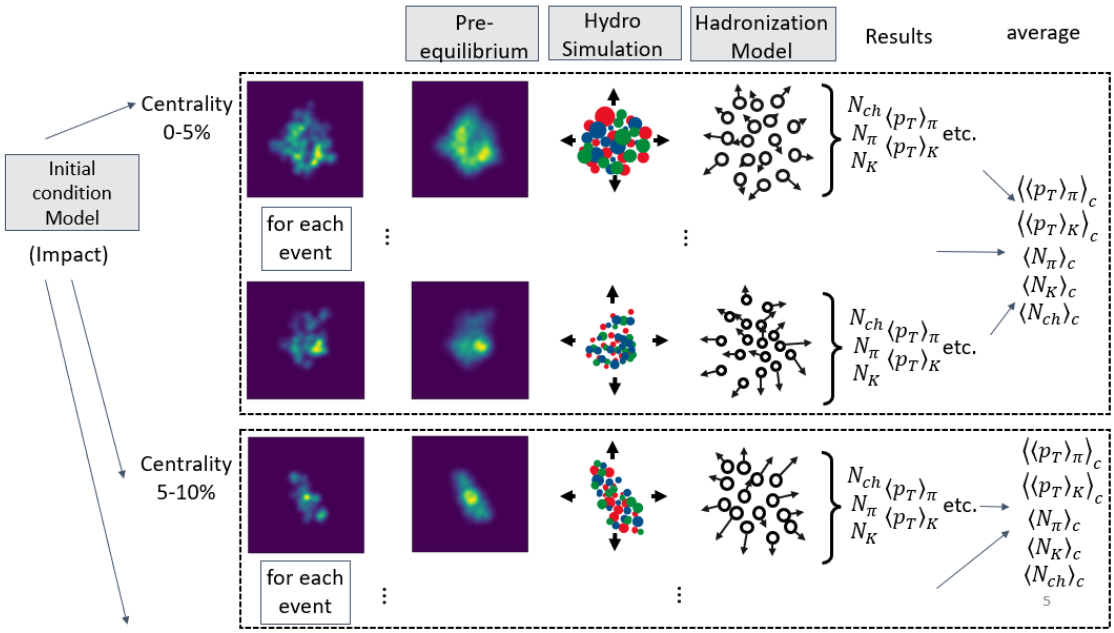

Figure 4: Structure of event-by-event simulations of heavy ion collisions

1.4 Scope and structure of the thesis

For this thesis, the initial condition model T$_\mathrm{R}$ENTo (see section 2.2) is employed. The hydrodynamic model Fluid*u*m (see section 2.5) is used for the hydrodynamic evolution (and the Cooper-Frye formula [15] for the freeze-out). To this point, the pre-equilibrium has been neglected for this procedure. The thesis will investigate the influence of the pre-equilibrium using a free streaming approximation of the dynamics (see section 2.3). The influence on total energy and entropy will be studied without specifying the exact execution of the hydrodynamic phase, but it will be taken into account that in Fluid*u*m a background-fluctuation splitting approach is considered. Comparison to an event-by-event approach will be drawn (see section 3.1). Further, the influence on charged particle multiplicity and charged particle mean momentum will be investigated using Fluid*u*m, and utilizing experimental results from ALICE as a reference (see section 3.2).
First, the models and the physical background used in the thesis will be explained. Then, the analysis will be carried out, and the results will be discussed.

2 Underlying Physics and Models

2.1 Equation of State

In order to find a thermodynamic description of a system, knowledge about its statistical behavior is required. In thermodynamic equilibrium, the statistical behavior can be expressed using the partition function Z, which describes the thermodynamic properties. With the partition function given, the Equation of State can be derived. The Equation of State connects thermodynamic quantities such as temperature, pressure, energy, etc. to each other.

For the thermodynamic description of the quark gluon plasma, the (2+1)-flavor QCD Equation of State [8] can be used, which is derived from lattice QCD calculations and well applicable in the temperature range of $T \in [130 - 400]MeV$. The pressure is given by

$$\frac{p(T)}{T^4} = \exp\left[-\frac{c^2}{(T/T_c)} - \frac{d^2}{(T/T_c)^2}\right]\left[\frac{\frac{(16+\frac{21}{2}N_f)\pi^2}{90} + a_1\left(\frac{T_c}{T}\right) + a_2\left(\frac{T_c}{T}\right)^2 + a_3\left(\frac{T_c}{T}\right)^3 + a_4\left(\frac{T_c}{T}\right)^4}{1 + b_1\left(\frac{T_c}{T}\right) + b_2\left(\frac{T_c}{T}\right)^2 + b_3\left(\frac{T_c}{T}\right)^3 + b_4\left(\frac{T_c}{T}\right)^4}\right] \tag{2}$$

a_1	-0.752335	a_2	-1.8151	a_3	-2.83317	a_4	4.20517	c	0.547521
b_1	-1.68716	b_2	7.83336	b_3	-13.3421	b_4	9.22752	d	0.0148163

Here $T_c \approx 154MeV$ is the critical temperature and $N_f = 3$ is the number of free quarks that are considered.

From Equ.(2), other thermodynamic quantities such as the energy density ϵ and the entropy density s can be derived. For large homogeneous media and vanishing Quark chemical potential, the QCD lattice system can be described using the grand canonical potential [16], which is connected to the partition function by $\Phi_G = -T \cdot ln(Z))$, leading to the equation

$$\frac{\epsilon(T) - 3p(T)}{T^4} = T\frac{\partial}{\partial T}(p(T)/T^4) \quad \Leftrightarrow \quad \frac{\epsilon(T)}{T^4} = T\frac{\partial}{\partial T}(p(T)/T^4) + \frac{3p(T)}{T^4} \quad . \tag{3}$$

This can be used in conjunction with $s(T) = (\epsilon(T) + p(T))/T$ (the Euler relation) to derive the link between p and ϵ or s. Due to the fact that the resulting functions $\epsilon(T)$ and $s(T)$ are strictly monotonically increasing, we can numerically define an interpolation function between $\epsilon(T)$ and $s(T)$.

2.2 T$_{\mathrm{R}}$ENTo

T$_{\mathrm{R}}$ENTo is a Monte Carlo model, which is able to simulate the deposition of entropy in a collision between a variety of ion pairs such as proton-proton collisions, Pb-Pb collisions, etc., but also the collisions of unequal ions such as Pb-p [17]. It is able to describe the entropy or energy deposition in the transverse plane (which is the plane that has its normal vector parallel to the beam direction).

Two projectiles, A and B are considered, which collide along the beam axis z. The position of the nucleons in both projectiles is sampled from a nucleon distribution, such as the Woods-Saxon distribution. Subsequently, via a probability distribution, the nucleons which take part in the collision i.e., the participants are chosen. For each participant i with the position (x_i, y_i, z_i), a participant thickness is defined

$$T_i(x, y) = w_i \int dz \rho_{proton}(x - x_i, y - y_i, z - z_i) \tag{4}$$

where w_i is an additional random weight factor drawn from a gamma distribution of unit mean and ρ_{proton} is the spatial distribution of one proton. The sum of T_i of all participants in A will give the thickness function T_A, the same holds for B. Finally, a reduced thickness function $f(x, y)$ is defined, which is assumed to be proportional to the deposited energy or entropy density. For the scope of this thesis, it is assumed that $f \propto dS/dy|_{\tau_0}$.
The reduced thickness function is defined as a generalized mean

$$f = T_R(p; T_A, T_B) = \left(\frac{T_A^p + T_B^p}{2} \right)^{1/p} \tag{5}$$

where p is chosen, to best describe the data. Note, that the form of the function allows for a scaling of the thickness functions cT_A and cT_B which will result in $T_R(p; cT_A, cT_B) = cT_R(p; T_A, T_B)$. This freedom of an additional scaling parameter allows relating the reduced thickness to a physical value of entropy $dS/dy|_{\tau_0} = cT_R(p; T_A, T_B)$.

The T$_{\mathrm{R}}$ENTo package can be found here [18].

2.3 Free Streaming

For a simple model of the early evolution of the non thermalized QGP a free streaming approach can be considered [10, 14]. The model gives an approximation of the transport of energy density. The initial energy density is seen as a field of massless partons. The initial transverse momentum distribution is assumed to be locally isotropic. A collisionless Bolzmann equation

$$p^\mu \partial_\mu f(x,p) = 0 \tag{6}$$

is employed in order to describe the evolution of the parton density field. In other words, a parton created in the collision at proper time τ_0 propagates in a given direction without interaction at the speed of light until the free streaming phase stops at the switching time τ_s.

For the system at hand, an appropriate set of coordinates is chosen:

Time is given by longitudinal proper time $\tau = \sqrt{t^2 - z^2}$. Therefore, the space-time hypersurface described by choosing a longitudinal proper time τ connects each spatial point at the beam axis to the local time of the lab frame. Note that the two proper times τ_0 and τ_s introduce a duration $\tau_s - \tau_0$ which is invariant of longitudinal boost. Therefore, each co-moving (reduced to longitudinal direction) reference frame experiences the same duration of free streaming evolution.
To describe spatial positions and movement, the system is separated into the transverse plane and longitudinal axis. Position on the transverse plane is given by the Cartesian coordinates $\mathbf{x}_T$, while movement on the transverse plane is given in polar coordinates of the momentum $\mathbf{p}_T = p_T \cdot (cosh(Y), cos(\phi_p), sin(\phi_p))$. Note that due to the vanishing mass of the partons, the velocity is directly connected to the momentum by

$$\mathbf{v}_T = (cos(\phi_p), sin(\phi_p)) \tag{7}$$

Position on the longitudinal axis is given by the space-time rapidity $\eta_s = \frac{1}{2} ln[(t+z)/(t-z)]$ and movement by rapidity $Y = \frac{1}{2} ln[(E+p_z)/(E-p_z)]$, which is a rewritten form of (1).

Dynamics

As stated before, the initial condition is seen as a density n of partons which now is dependent on position and dependent on the parton momentum $n(x_T, y_T, \eta, p_T, \phi_p, Y, \tau_0)$. When only looking at the central rapidity region, one can assume boost invariance, and

can neglect η and Y.
Now for the density of partons $n(x_T, y_T, \phi_p, p_T, \tau_s)$ on the transverse plane, due to the non-interacting nature of the partons this density can be related to the initial density at τ_0 via the equation

$$n(x_T, y_T, \phi_p, p_T, \tau_s) = n(x_T - (\tau_s - \tau_0) \cdot cos(\phi_p), y_T - (\tau_s - \tau_0) \cdot sin(\phi_p), \phi_p, p_T, \tau_0) \quad (8)$$

using the fact that in the co moving transverse plane the velocity of those partons is given by Equ. (7) for all particle momenta p_T.
In relativistic dynamics, the energy density is described as part of the symmetric stress energy tensor $T^{\mu\nu}$. The stress energy tensor can be calculated from the density distribution n with the equation (see [10])

$$T^{\mu\nu}(x_T, y_T, Y = 0, \tau_s) = \int dp_T d\phi_p p_T^\mu p_T^\nu n(x_T - (\tau_s - \tau_0) \cdot cos(\phi_p), y_T - (\tau_s - \tau_0) \cdot sin(\phi_p), \phi_p, p_T, \tau_0) \quad (9)$$

A factorization approach can be applied to the particle distribution, so that

$$\begin{aligned} & n(x_T - (\tau_s - \tau_0) \cdot cos(\phi_p), y_T - (\tau_s - \tau_0) \cdot sin(\phi_p), \phi_p, p_T, \tau_0) && (10) \\ & = n(x_T - (\tau_s - \tau_0) \cdot cos(\phi_p), y_T - (\tau_s - \tau_0) \cdot sin(\phi_p), \phi_p, \tau_0) && (11) \\ & \cdot f(x_T - (\tau_s - \tau_0) \cdot cos(\phi_p), y_T - (\tau_s - \tau_0) \cdot sin(\phi_p), p_T, \tau_0) && (12) \end{aligned}$$

with f defining the distribution of momentum magnitude.
In the very simple case where this distribution is independent on the spatial position, we can simplify Equ. (9) to

$$\begin{aligned} & T^{\mu\nu}(x_T, y_T, Y = 0, \tau_s) && (13) \\ & = \int_0^\infty dp_T f(p_T) p_T^2 \cdot \int_0^{2\pi} d\phi_p \hat{p_T}^\mu \hat{p_T}^\nu n(x_T - (\tau_s - \tau_0) \cdot cos(\phi_p), y_T - (\tau_s - \tau_0) \cdot sin(\phi_p), \phi_p, \tau_0) && (14) \end{aligned}$$

with $\hat{p_T} = \mathbf{p_T}/p_T$.
To account for longitudinal expansion, the tensor is scaled with a factor of $1/(\tau_s - \tau_0)$, which arises from the Bjorken flow [19].

The free streaming package used in this thesis can be found here [20].

2.4 Landau Matching Procedure

Let us consider now a field of stress energy tensors $T^{\mu\nu}(x_T, y_T, Y = 0, \tau_s)$ which describe the state of the system at the proper time of the transition from pre-equilibrium to fluid phase. The fluid after the transition is in local equilibrium. Furthermore, by transitioning to a fluid, quantities like pressure, fluid velocity and transport coefficients have to be introduced. This is captured by the Landau Matching Procedure.
To understand this procedure, one has to understand the properties of the system, hence also the stress energy tensor $T^{\mu\nu}$. In the following section, the Landau matching will be explained for a 4×4 stress energy tensor. Note that for the application in this thesis we can neglect one spatial direction, i.e. the beam direction.

The components of $T^{\mu\nu}$ are bound to specific physical properties of the system (see Fig. 5), that generally also constrain it to be symmetrical.

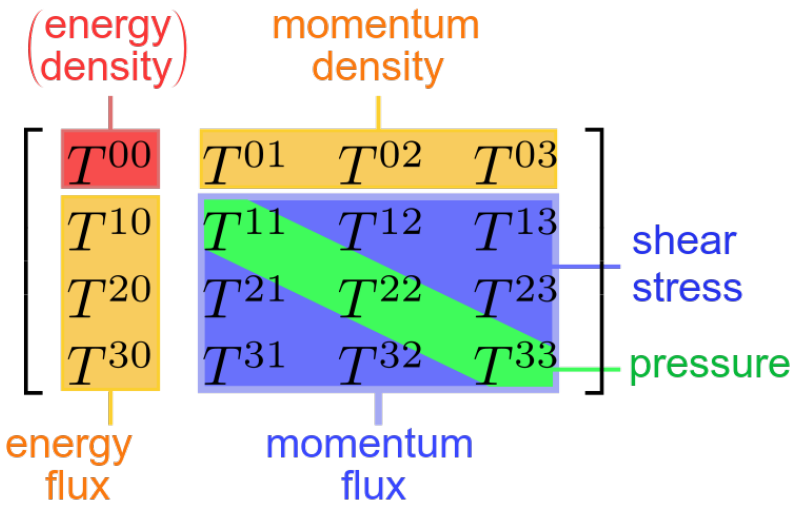

Figure 5: Structure of the stress energy tensor $T^{\mu\nu}$

As an example for the ideal fluid at rest one finds, that the stress energy tensor has the form

$$T^{\mu\nu} = \begin{pmatrix} \epsilon & 0 & 0 & 0 \\ 0 & p & 0 & 0 \\ 0 & 0 & p & 0 \\ 0 & 0 & 0 & p \end{pmatrix} \tag{15}$$

The tensor can be transformed using an element Λ of the Lorenz group with its time component u^μ. When transformed out of the rest frame using Λ the tensor can be written

as

$$T^{\mu\nu} = \epsilon u^{\mu} u^{\nu} + p\,(u^{\mu} u^{\nu} + g^{\mu\nu}) \tag{16}$$

with ϵ as the energy density and p the pressure. In viscous fluid dynamics, the stress-energy tensor is generally written in the covariant form

$$T^{\mu\nu} = \epsilon u^{\mu} u^{\nu} + (p + \pi_{bulk})(u^{\mu} u^{\nu} + g^{\mu\nu}) + \pi^{\mu\nu} \tag{17}$$

In this notation u^{μ} is the local fluid-4-velocity and ϵ is the energy density in the co-moving reference frame. The total pressure is given by $p + \pi_{bulk}$ and where p is connected to ϵ via the Equations of State. π_{bulk} and $\pi^{\mu\nu}$ describe the deviations from the ideal fluid with π_{bulk} being the bulk viscous pressure and $\pi^{\mu\nu}$ being the shear stress tensor. The bulk viscous pressure acts for or against isotropic changes in volume of the fluid, while $\pi^{\mu\nu}$ acts upon shearing of fluid layers. $\pi^{\mu\nu}$ is orthogonal to the fluid velocity ($\pi^{\mu}_{\ \nu} u^{\nu} = 0$), symmetric and traceless ($\pi^{\mu}_{\ \mu} = 0$). Furthermore, in the notation of this thesis the metric is $g_{\mu\nu} = diag(-1, 1, 1, 1)$ and the normalization of the fluid velocity is therefore negative ($u^{\mu} u_{\mu} = -1$).
The decomposition of the tensor identifies the viscous effects as the deviations to the perfect fluid. Further, the Equation of State is defined in the rest frame of a fluid cell and therefore the decomposition enables the introduction of pressure along with the velocity of the fluid cell.

The movement of fluid is in the classical picture the net flux of the particles that are contained in a fluid cell. However, especially in relativistic hydrodynamics, sometimes movement of energy density and movement of particle number or other conserved charges are not equal. It is therefore to specify what movement is described by the rest frame. The frame that describes the movement of particles or conserved charges is called the "Eckart frame", while the movement of energy is captured by the "Landau frame" [21]. Therefore, the rest frame defined with u^{μ} is the Landau frame which will be used in this thesis as the "rest frame" of the fluid.
As described before (Fig. 5), the tensor components $T^{\mu 0}$ refer to the energy flux. In the landau frame the spatial flux vanishes and therefore $T^{\mu 0}$ reads $(\epsilon, 0, 0, 0)$, implying:

$$T'^{\mu\nu} = \begin{pmatrix} \epsilon & 0 & 0 & 0 \\ 0 & T^{11} & T^{12} & T^{13} \\ 0 & T^{21} & T^{22} & T^{23} \\ 0 & T^{31} & T^{32} & T^{33} \end{pmatrix} \tag{18}$$

Due to the fact, that the tensor is symmetric the spatial entries can be diagonalized using spatial rotations and thus the tensor has its diagonal form in the Landau frame. For the diagonalization processes the $O^+(1;3)$ group is used, which in Minkowski space-time is identifiable with the proper Lorenz group. Thus, the diagonalization yields 4 eigenvectors, where three are space-like and one is time-like. The time-like eigenvector will be the time component of the respective transformation and thus the velocity which defines the boost into the Landau frame, i.e. the fluid velocity u^μ. The eigenvalue of u^μ will be ϵ. This is called the Landau condition:

$$T^\mu_\nu u^\nu = \epsilon u^\mu \tag{19}$$

Knowing ϵ, the pressure p can be derived using the Equation of State. Bulk pressure and the shear stress form a tensor

$$\Pi^{\mu\nu} = \pi_{bulk}(u^\mu u^\nu + g^{\mu\nu}) + \pi^{\mu\nu} = T^{\mu\nu} - [\epsilon u^\mu u^\nu + p\,(u^\mu u^\nu + g^{\mu\nu})] \tag{20}$$

The tensor $\Pi^{\mu\nu}$ is per definition orthogonal to the fluid velocity and can be split into a traceless part $\pi^{\mu\nu}$ and the trace part $(u^\mu u^\nu + g^{\mu\nu})Tr(\Pi)$ with $Tr(\Pi)/3 = \pi_{bulk}$.

2.5 Fluid*u*m

For the hydrodynamic description, the model Fluid*u*m [22] is used. For the model, nearly the same coordinate system is chosen as described in section 2.3. However, Fluid*u*m exploits not only symmetries in Bjorken boosts, but also azimuthal symmetries. Therefore, the spatial coordinates for the transverse plane are given in polar coordinates r and ϕ with $(x, y) = (r \cdot cos(\phi), r \cdot sin(\phi))$.
The simulation approach of Fluid*u*m differs fundamentally from an event-by-event simulation, which was described earlier in Fig. 4.
The differential equations considered for the evolution are causal quasi-linear partial differential equations

$$\mathbf{A}(\mathbf{\Phi}, \tau, r)\cdot\partial_\tau\mathbf{\Phi}+\mathbf{B}(\mathbf{\Phi}, \tau, r)\cdot\partial_r\mathbf{\Phi}+\mathbf{C}(\mathbf{\Phi}, \tau, r)\cdot\partial_\phi\mathbf{\Phi}+\mathbf{D}(\mathbf{\Phi}, \tau, r)\cdot\partial_\eta\mathbf{\Phi}-\mathbf{S}(\mathbf{\Phi}, \tau, r) = 0. \quad (21)$$

The local description is given by $\mathbf{\Phi}$, which is a N dimensional vector containing independent values for the fluid description such as local temperature, fluid velocity, bulk pressure and shear stress. A, B, C and D are $N \times N$ coefficient matrices and S is a N dimensional vector that defines the inhomogeneous part of the equation.
Furthermore, the approach considers an expansion using a background-fluctuation splitting, where the field $\mathbf{\Phi}$ is split into a background part $\mathbf{\Phi_0}$ and a series of fluctuation fields $\mathbf{\Phi_1}$. Another precondition applied, is that the fluctuations are small enough for ϕ and η in respect to the background, thus allowing for the expansion

$$\mathbf{\Phi}(\tau, r, \phi, \eta) = \mathbf{\Phi_0}(\tau, r) + \epsilon\mathbf{\Phi_1}(\tau, r, \phi, \eta) \quad (22)$$

One condition that must be satisfied, is that the background is symmetric in ϕ and η. One can achieve this for example with the help of statistical symmetries, where the background is seen as an average state of a field over a number of given events. A very suitable ensembles of events used are centrality classes, due to the fact that experimental results are given in event-averaged quantities of events in a centrality class (see Fig. 6). This heavily reduces the computational effort, which in case of hydrodynamic simulations for heavy-ion collisions is usually considerably huge. Therefore, studying this approach is of great interest, since computational resources are scarce.

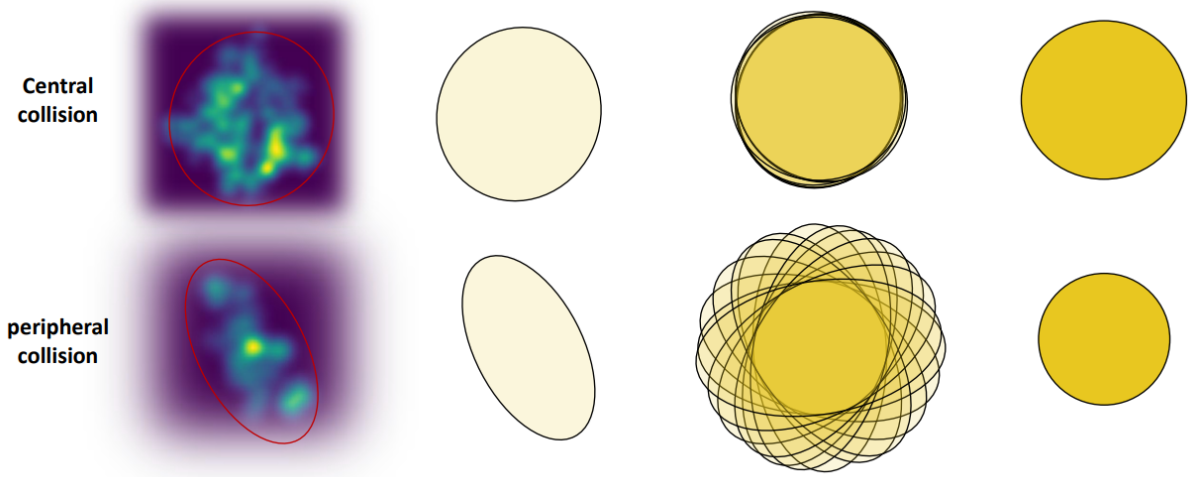

Figure 6: Graphical representation of how background fields, which are symmetric in ϕ, are retrieved from single events which do not possess azimuthal symmetry. This process also creates a symmetry in η, which is not captured in this graphical representation

For measurements that are independent of ϕ and η such as for example the mean charged particle multiplicity N_{ch} or the mean transverse momentum of charged particles $\langle p_T \rangle$, the solution for the background field can be used. For quantities like for example flow parameters, which are dependent on ϕ, the solution of the background field does not suffice, and the fluctuation fields have to be taken into account.

In this thesis, only event-averaged quantities, that can be calculated with the solution of the background field, will be considered. Thus, the procedure for the simulation that was given before (Fig. 4), which is used for event-by-event simulation has to be adjusted to the approach (see Fig. 7)

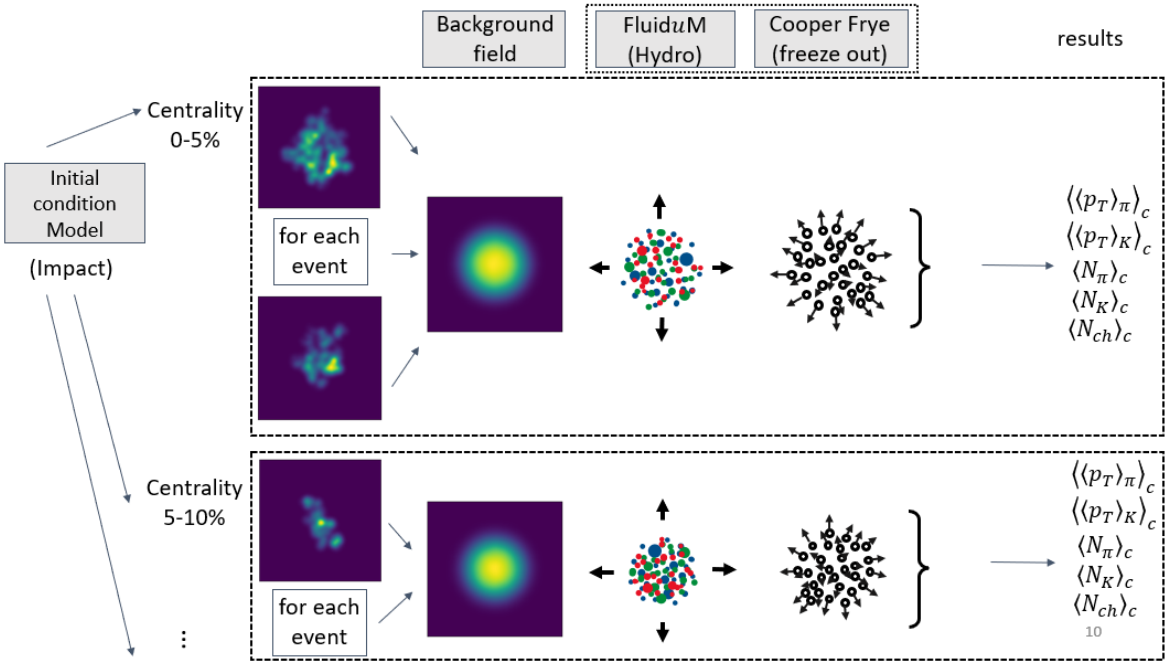

Figure 7: Simulation procedure used to simulate results from Heavy Ion Collisions with Fluid*u*m from the background field.

Note, that in Fluid*u*m the hadronization is already implemented using the Cooper Frye formula, which will not be further discuss in this thesis, for references one can look at [15]. Furthermore, the decay of the produced particles is simulated with the FastReso model [23].

What will be now of specific interest in this thesis is, what happens when a free streaming pre-equilibrium is added to the simulation scheme in Fig. 7. The free streaming evolution will be introduced to the model in the following way (see Fig. 8):

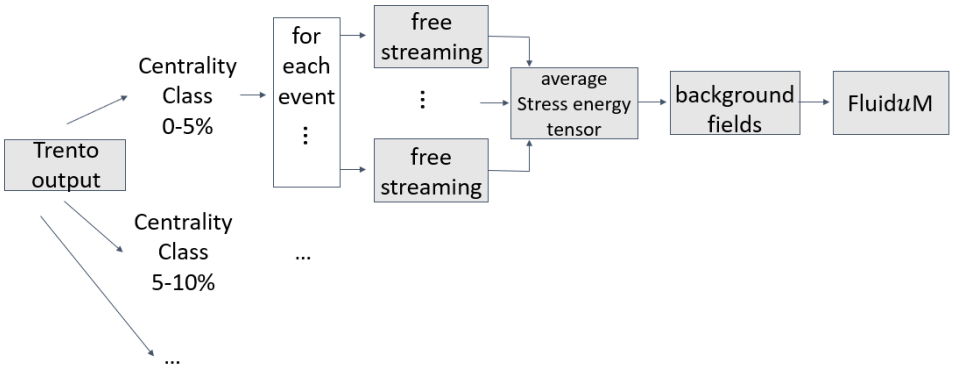

Figure 8: Simulation schematic for the implementation of free streaming to Fluid*u*m

2.6 Properties of nearly perfect fluids

The hydrodynamic phase, which is applied after free streaming, has been found out to employ very low values for viscosity over entropy η/s [24]. In general, this means that the dynamics are ruled by nearly inviscid hydrodynamics and the QGP behaves close to a perfect liquid. In fact, it is found that the QGP is the most perfect fluid found so far in nature [25, 26]. In a perfect liquid, not only energy is conserved, but also entropy. This implies, for one of course, that the total energy present after thermalization will be the same as the total energy that is ejected in the form of particles out of the collision. For the other, it implies, that also the total entropy of the system after freeze-out will be nearly equal to the total entropy of the system after thermalization. The total energy and entropy can be calculated with

$$E = \int T^{0\mu} d\Sigma_\mu \tag{23}$$

$$S = \int s(\epsilon) u^\mu d\Sigma_\mu \qquad [27]. \tag{24}$$

The hyper surface element $d\Sigma_\mu$ is, in the case of a space-like surface defined by a constant proper time τ, given by $d\Sigma_\mu = (\tau dx dy d\eta, 0, 0, 0)$ [28]. In the case of boost invariance, we can neglect the dependence of the integrand on η and the integration of η drops out.
Additionally, at freeze-out the total entropy is linearly proportional to the charged particle multiplicity of a collision and the total energy can also be related linearly to mean transverse momentum [29, 30, 31]. Using the conservation laws and the linear dependence of observables, one can already estimate properties of the system at freeze-out, without specifying the form of the hydrodynamic model, as long as it exhibits sufficiently low viscosities.

3 Impact of free streaming on initial conditions

In the first part of the analysis, the influence of a free streaming pre-equilibrium evolution on initial conditions will be examined. Total energy and total entropy of fields defining the start condition for the hydrodynamic phase, i.e. the background fields (see Fig. 8) and the separately free-streamed events (see Fig. 4), will be calculated. As stated before in section 2.5, the value for total energy and total entropy resembles an event-average of the events in the centrality class connected to the background field. Calculating the event-average of total energy and total entropy for the separately free-streamed events will allow comparing the background-splitting approach to the event-by-event approach. Data acquisition is performed event-by-event, therefore the event-by-event result for total energies and total entropies can be seen as close to the "true" values that are present in experiments. This section provides a motivation to implement a pre-equilibrium phase before the relativistic fluid dynamics phase when using a background-fluctuation splitting approach.

3.1 Investigating non free-streamed initial conditions

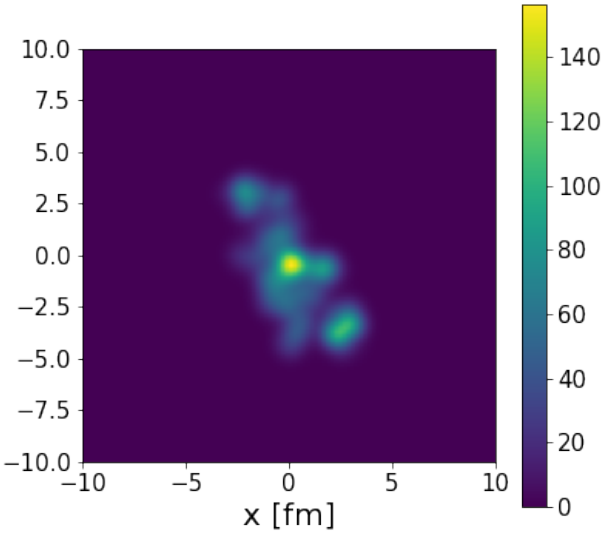

Figure 9: An initial condition provided by TRENTo simulating a Pb-Pb collision with default configuration (for the default configuration, see the documentation [32]).

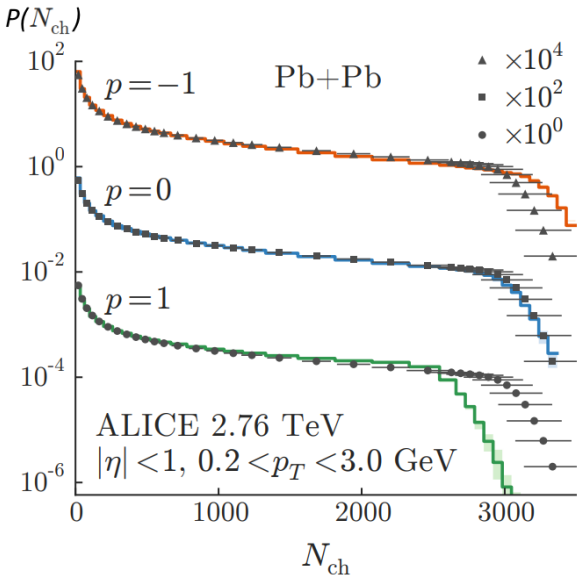

Figure 10: Distribution of charged particle multiplicity given by TRENTo for different reduced thickness parameters p compared to distribution found in ALICE data (Fig. from [17]).

The Monte Carlo model T$_{\mathrm{R}}$ENTo [17] is used to create initial conditions on the transverse plane. These initial conditions are given in a 100 × 100 cell grid, where each grid cell has the dimensions 0.2 fm × 0.2 fm (see Fig.9)

The profile provided by T$_{\mathrm{R}}$ENTo can be interpreted as an energy density field or an entropy density field. With a reduced thickness parameter of $p = 0$ T$_{\mathrm{R}}$ENTo already produces the correct distribution of multiplicity of charged particles for Pb-Pb collisions at $\sqrt{s_{NN}}$ =2.76 TeV (see Fig. 10). Furthermore, the charged particle multiplicity distribution in a heavy-ion collision is related almost linearly to the total entropy distribution. Using these two properties, for this analysis it was chosen to relate the T$_{\mathrm{R}}$ENTo output to an initial entropy density field via a normalization factor.

To determine the correct normalization factor, the total entropy of an initial state in the 0-5% centrality class is matched to the total yield of charged particles in the same centrality class measured by the ALICE collaboration [33].

After sorting 1×10^6 events into 100 centrality classes, the mean value of total entropy of the highest centrality class can be determined. This results in a scaling factor of 68.8, which is applied to match the entropy fields in all centrality classes.
To mimic the conditions of a HIC, the initial entropy profiles calculated with T$_{\mathrm{R}}$ENTo are rotated by a random angle on the transverse plane.

3.1.1 Background-fluctuation splitting on T$_{\mathrm{R}}$ENTo initial conditions

The state of the system is described by the stress-energy tensor field. Up to the point of the hydrodynamic evolution, a grid with indices $i, j \in \{1, ..., 100\}$ is considered. In each cell, the thermodynamics quantities and fluid dynamics are described by the Equation of State and the local shear stress tensor $T^{\mu\nu}_{(i,j)}$.

In order to perform a background-fluctuation splitting on the initial fields at hand, the average of the fields for each centrality class has to be considered. In the case of the previously computed one million events divided into 100 centrality classes, one has to determine 100 background-field profiles.
The fields in each centrality class can be defined just by the entropy density field and the Equation of State, due to the fact that the fluid is considered to be initially at rest ($u^\mu = (1, 0, 0)$) in the transverse plane. Note, that from now the spatial components are reduced to two dimensions, i.e. the transverse plane.
Background fields for energy density, temperature, etc. can be derived via the Equation

of State. The initial bulk viscous pressure of π_{bulk} and shear stress components $\pi^{\mu\nu}$ are zero.
In the next section, the total energy and total entropy of a non free-streamed background field will be investigated and the event-averaged quantities will be compared to an event-by-event approach. We consider the case $\tau_s = 1\text{fm/c}$, which is the right order of magnitude for the thermalization time [10].

At this point, it is useful to redirect to Section 2.6, where the description of total energy and total entropy for a continuous field was given by Eq. (23).

Single event

For a fluid at rest in the transverse plane ($u^\mu = (1, 0, 0)$) at $\tau = 1\text{fm/c}$, the energy density in the lab frame reads $T^{00}_{(i,j)} = \epsilon_{(i,j)}$ and the space-like hyper surface $d\Sigma_\mu$ reads $(dxdy, 0, 0)$. Thus, the total energy and entropy can be calculated with

$$E = \int\int \epsilon(s) \cdot dxdy \quad \rightarrow \quad E = \sum_{i=1}^{N}\sum_{j=1}^{N} \Delta A \cdot \epsilon(s_{(i,j)}) \tag{25}$$

$$S = \int\int s \cdot dxdy \quad \rightarrow \quad S = \sum_{i=1}^{N}\sum_{j=1}^{N} \Delta A \cdot s_{(i,j)} \tag{26}$$

using the normalized entropy density field s, the cell area ΔA and the dimensions of the grid (N =100).

Event average

It will be differentiated between "true" event-average of total energy or entropy $\langle E\rangle_{true}, \langle S\rangle_{true}$ which is calculated in event-by-event simulations and event-averaged total energy or entropy, determined from the background field $\langle E\rangle_{background}, \langle S\rangle_{background}$. The latter quantities will be defined by averaging over N_{ev} =10 000 events (denoted with the index n_{ev}) for each centrality class, with a total of N_{cen} =100 classes (denoted with the index n_{cen}).

The background fields $\bar{s}_{n_{cen}}$ and $\bar{\epsilon}_{n_{cen}}$ are defined as

$$\bar{s}_{n_{cen},(i,j)} = \sum_{n_{ev}=1}^{N_{ev}} s_{n_{cen},n_{ev},(i,j)}/N_{ev} \tag{27}$$

$$\bar{\epsilon}_{n_{cen},(i,j)} = \epsilon\left(\sum_{n_{ev}=1}^{N_{ev}} s_{n_{cen},n_{ev},(i,j)}/N_{ev}\right) \tag{28}$$

The total energy and entropy from the background field already resembles an event averaged quantity. The "true" event average of total energy and entropy is the arithmetic average of the calculated quantities from every event considered in the centrality class.

$$\langle E\rangle_{true\ n_{cen}} = \sum_{n_{ev}=1}^{N_{ev}}\sum_{i=1}^{N}\sum_{j=1}^{N}\Delta A\cdot\epsilon(s_{n_{cen},n_{ev},(i,j)})/N_{ev} \tag{29}$$

$$\langle S\rangle_{true\ n_{cen}} = \sum_{n_{ev}=1}^{N_{ev}}\sum_{i=1}^{N}\sum_{j=1}^{N}\Delta A\cdot s_{n_{cen},n_{ev},(i,j)}/N_{ev} \tag{30}$$

$$\langle E\rangle_{background\ n_{cen}} = \sum_{i=1}^{N}\sum_{j=1}^{N}\Delta A\cdot\bar{\epsilon}_{n_{cen},(i,j)} = \sum_{i=1}^{N}\sum_{j=1}^{N}\Delta A\cdot\epsilon\left(\sum_{n_{ev}=1}^{N_{ev}} s_{n_{cen},n_{ev},(i,j)}/N_{ev}\right) \tag{31}$$

$$\langle S\rangle_{background\ n_{cen}} = \sum_{i=1}^{N}\sum_{j=1}^{N}\Delta A\cdot\bar{s}_{n_{cen},(i,j)} = \sum_{i=1}^{N}\sum_{j=1}^{N}\Delta A\cdot\sum_{n_{ev}=1}^{N_{ev}} s_{n_{cen},n_{ev},(i,j)}/N_{ev} \tag{32}$$

Here one can directly see that (30)= (32), but (29)≠ (31) since the Equation of State is non-linear.
In the next section, this inequality will be further explained.

3.1.2 Inequality of total energy from event-by-event and background field calculations

For simplicity, an ideal Equation of State ($e(s) \propto s^{4/3}$ [34]) is considered. This is supported by the fact, that in the high-temperature limit, the employed Equation of State (see Section 2.1) approaches the non-interacting regime of an ideal gas [8].

As can be seen in Eq. (29) and Eq. (31) the integrals differ because

$$\sum_{n_{ev}=1}^{N_{ev}}\epsilon(s_{n_{cen},n_{ev},(i,j)})/N_{ev} \neq \epsilon(\sum_{n_{ev}=1}^{N_{ev}} s_{n_{cen},n_{ev},(i,j)}/N_{ev}) \tag{33}$$

Again for the sake of simplicity in this section the indices n_{cen} and (i, j) are omitted. Now, the total field can be described as a combination of background field and fluctuation field as described in Section 2.5 with:

$$s_{n_{ev}} = \bar{s} \cdot (1 + \delta s_{n_{ev}}) \tag{34}$$

where $\bar{s}$ is the background field as defined in Eq. (27) and δs a fluctuation field.
When the ideal gas equation is plugged into Eq. (33) for the left and right-hand side of the inequality (LHS, RHS), one finds

$$\text{LHS } (\langle E \rangle_{true}) : \quad \sum_{n_{ev}=1}^{N_{ev}} (\bar{s} \cdot (1 + \delta s_{n_{ev}}))^{4/3} / N_{ev} \tag{35}$$

$$\text{RHS } (\langle E \rangle_{background}) : \quad (\sum_{n_{ev}=1}^{N_{ev}} \bar{s} \cdot (1 + \delta s_{n_{ev}}) / N_{ev})^{4/3} \tag{36}$$

The right side can be easily simplified by using the definition of $\bar{s}$ in Eq. (27) and using the fact the $\langle \delta s \rangle = 0$ by definition:

$$\text{RHS} = \quad \bar{s}^{4/3} \tag{37}$$

Of the left side, a Taylor expansion can be considered around $\delta s_{n_{ev}} = 0$:

$$\text{LHS} = \quad \bar{s}^{4/3} \cdot (1 + \frac{4}{3} \sum_{n_{ev}=1}^{N_{ev}} \delta s_{n_{ev}} / N_{ev} + \frac{2}{9} \sum_{n_{ev}=1}^{N_{ev}} \delta s_{n_{ev}}^2 / N_{ev} + \frac{4}{81} \sum_{n_{ev}=1}^{N_{ev}} \delta s_{n_{ev}}^3 / N_{ev} + ...) \tag{38}$$

$$= \quad \bar{s}^{4/3} \cdot (1 + \frac{2}{9} \langle \delta s^2 \rangle + \frac{4}{81} \langle \delta s^3 \rangle + \mathcal{O}(\langle \delta s^4 \rangle)), \tag{39}$$

What can be seen is that the deviation between Eq. (29) and Eq. (31) is dependent on the magnitude of the fluctuations. Therefore, a stronger fluctuation field will lead to a stronger deviation.

3.1.3 Ratio $\langle E \rangle_{background}/\langle E \rangle_{true}$ from T$_{\mathrm{R}}$ENTo initial conditions

Using a set of 1×10^6 events divided into 100 centrality classes, the ratio $\langle E \rangle_{background}/\langle E \rangle_{true}$ (see Eq. (29) and Eq. (31)) is plotted in dependence of the centrality class (see Fig.11).

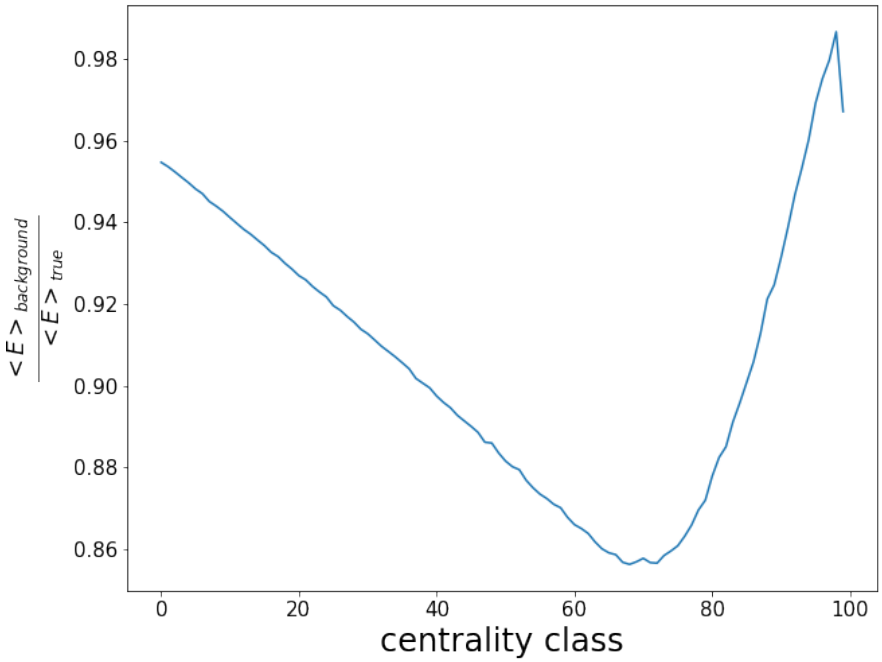

Figure 11: Ratio of $\langle E \rangle_{background}/\langle E \rangle_{true}$ in dependence of centrality class ($N_{ev} = 1000$ and $N_{cen} = 100$)

Here, the deviation between the total energy determined by event-by-event simulations and the total energy calculated using background fields can be observed. As expected, the deviation gets stronger with decreasing centrality, because in peripheral collisions the normalized fluctuation fields are generally larger than the ones in central collisions: At higher impact parameter, the shape of the excited region gets more elliptical and thus azimuthally asymmetric. The total energy from the background field of T$_{\mathrm{R}}$ENTo initial conditions seems to be underestimated. The best agreement is reached at high centrality, with about 5% underestimation. In the centrality classes near 70%, the deviation reaches up to around 15%.

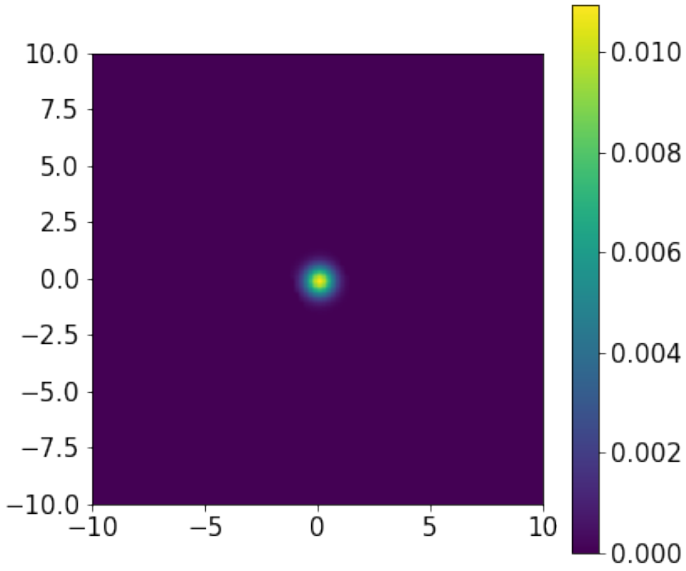

Figure 12: Energy density field of an ultra peripheral collision (99-100% centrality class) energy density is given in GeV fm^{-3}

What can be seen in very peripheral events is an increase in the ratio. A plausible explanation, is that for very peripheral collisions the produced fields recover their azimuthal symmetry (see Fig. 12), which in turn would strongly reduce the fluctuations and therefore the discrepancy between $\langle E \rangle_{background}$ and $\langle E \rangle_{true}$.

3.2 Investigating free-streamed initial conditions

The free streaming evolution takes an energy density field at rest, so directly at the time of collision ($\tau = 0$, where T$_\mathrm{R}$ENTo initial conditions are used), and evolves it to a given proper time τ_s (see section 2.3).
The field resulting from the free streaming evolution is the stress-energy tensor field as described in 3.1.1. The stress-energy tensors are normalized by a factor of $1/\tau_s$, which accounts for the longitudinal Bjorken expansion of the fireball during the pre-equilibrium evolution [19]. A further normalization has to be considered, due to the fact that after free streaming the average entropy in a given centrality class is changed by the landau matching procedure. This change is dependent on the switching time τ_s, which is also stated in [14]. In order to again obtain the correct mean multiplicity for the highest centrality class, the T$_\mathrm{R}$ENTo initial conditions must be normalized such that after free streaming the correct event-averaged total entropy is given for the most central collisions. Note that this normalization is then dependent on the free streaming time τ_s. The normalization also differs between the background fields and single events, because total entropy is calculated differently for free-streamed background fields and for free-streamed single events, as will become apparent in the next sections.

As explained in section 2.4, the fluid fields, i.e. $\epsilon_{(i,j)}(\tau_s)$, $u^\mu_{(i,j)}(\tau_s)$, $\pi_{bulk}(\tau_s)$ and $\pi^{\mu\nu}_{(i,j)}(\tau_s)$ can be extracted via the Landau matching procedure.
In this chapter and the following ones, the shear stress tensor $\pi^{\mu\nu}_{(i,j)}(\tau_s)$ and bulk viscous pressure π_{bulk} is neglected. The main contributions that define the initial state come from the fields of fluid velocity u^μ and the local (co-moving reference frame) thermodynamic conditions in the respective fluid cells, given by $\epsilon_{(i,j)}(\tau_s)$. However, it is worth to investigate the influence of the initial shear stress and bulk viscous pressure on Fluid*u*m in future studies.

As a comment on notation: The fluid velocity of the fluid cells can be expressed via $v_r = \sqrt{(u^0)^2 - 1}/u^0$, which in other words is just the difference between describing the magnitude of the fluid velocity seen from the lab frame with the β rather than the Lorentz γ. The expression of fluid velocity as v_r is also later necessary, because Fluid*u*m uses v_r as the initial fluid velocity.
Fig. 13 shows the fields of $\epsilon_{(i,j)}(\tau_s)$ and $v_{r(i,j)}$ with no free streaming and with free streaming.

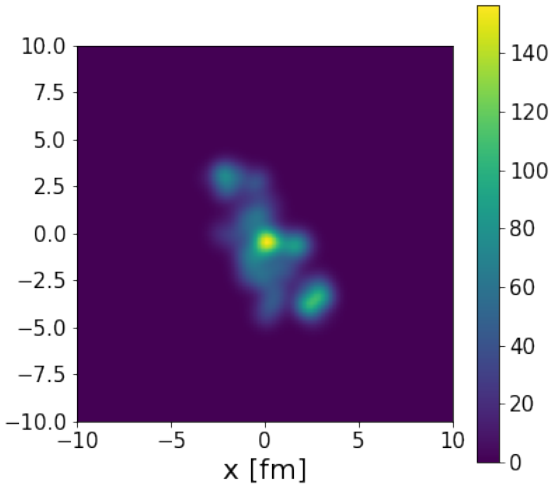

(a) energy density ϵ from T$_\mathrm{R}$ENTo

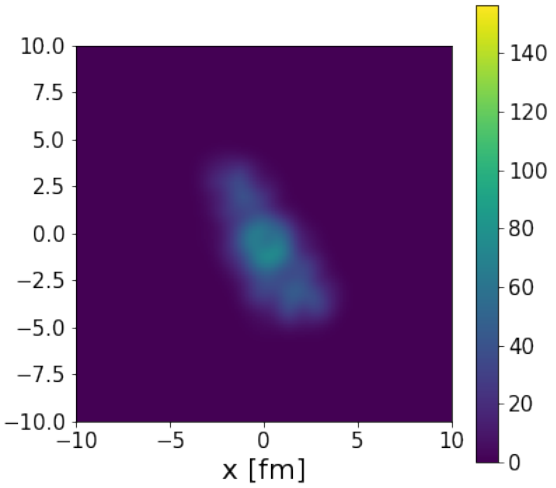

(b) energy density ϵ at $\tau_s = 1\mathrm{fm/c}$

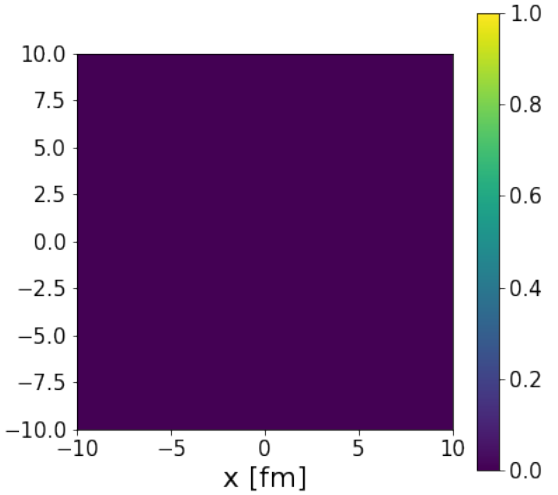

(c) fluid velocity v_r from T$_\mathrm{R}$ENTo

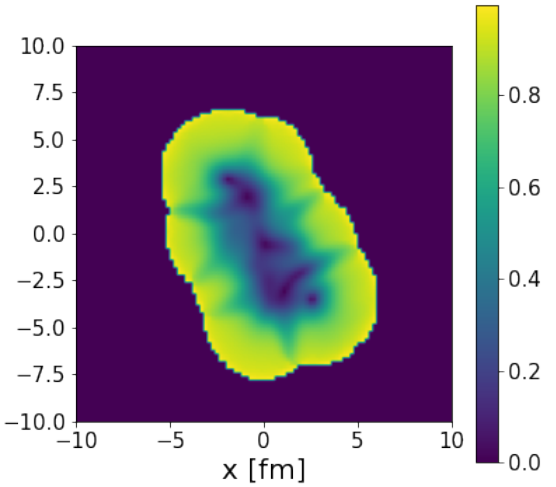

(d) fluid velocity v_r at $\tau_s = 1\mathrm{fm/c}$

Figure 13: Effect of free streaming on T$_\mathrm{R}$ENTo initial conditions. On the left side no free streaming is used, on the right side free streaming was applied up to $\tau_s = 1\mathrm{fm/c}$. The fluid velocities are given in natural units. The energy densities are given in GeV fm^{-3}

as can be seen, the fluid velocity builds up during the free streaming pre-equilibrium phase. In addition, the local energy density field seems to smooth out. This implies a reduction in the normalized fluctuation field, as discussed in section 3.1.2, as the field gets more symmetric. This assumption will later be verified (in section 3.2.3).

3.2.1 Background-fluctuation splitting on free-streamed initial conditions

As it was done in section 3.1.1, one million events divided into 100 centrality classes are examined. Due to the fact that the fluid builds up fluid velocity during the pre-equilibrium phase, one cannot directly use Eq. (29-32) to compute averages.
In each centrality class n_{cen} the background fields for $\epsilon_{(i,j)}(\tau_s)$ and $v_{r(i,j)}(\tau_s)$ are obtained using the Landau matching procedure (see section 2.4) on the average shear stress tensor field $\overline{T^{\mu\nu}}_{n_{cen},(i,j)}(\tau_s)$:

$$\overline{T^{\mu\nu}}_{n_{cen},(i,j)}(\tau_s) = \sum_{n_{ev}=1}^{N_{ev}} T'^{\mu\nu}_{n_{cen},n_{ev},(i,j)}(\tau_s)/N_{ev} \tag{40}$$

with N_{ev} =10 000.
The prime symbol on the stress energy tensors should be a reminder, that the background fields use a different normalization. Hence, the single event fields $T^{\mu\nu}_{n_{cen},n_{ev},(i,j)}(\tau_s)$ are not equal to the fields used to form the background field:

$$T^{\mu\nu}_{n_{cen},n_{ev},(i,j)}(\tau_s) \neq T'^{\mu\nu}_{n_{cen},n_{ev},(i,j)}(\tau_s) \tag{41}$$

In each centrality class the background fields extracted from $\overline{T^{\mu\nu}}_{n_{cen},(i,j)}(\tau_s)$ will be denoted as $\overline{\epsilon_{n_{cen},(i,j)}}(\tau_s)$ and $\overline{v_{r\,n_{cen},(i,j)}}(\tau_s)$. Notice that this procedure coincides with Eq. (29-32) in the case of a fluid at rest (as the one in absence of a free streaming). Examples of the background fields for energy density and fluid velocity can be seen in Fig. 14. One observes, that in the center of the fireball the fluid is nearly at rest while at the edges the fireball picks up more fluid velocity.

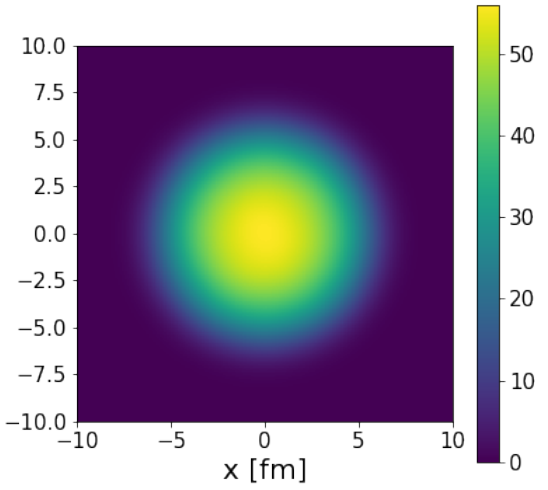

(a) energy density $\bar{\epsilon}$ $0-1\%$

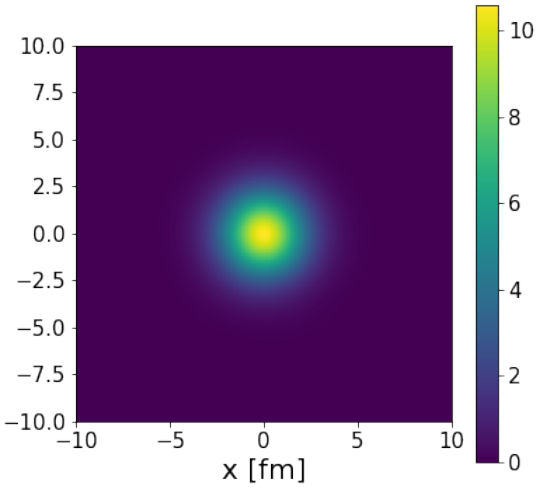

(b) energy density $\bar{\epsilon}$ $60-61\%$

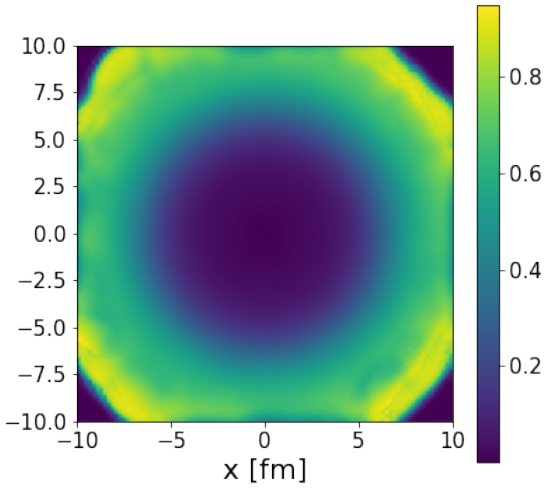

(c) fluid velocity $\overline{v_r}$ $0-1\%$

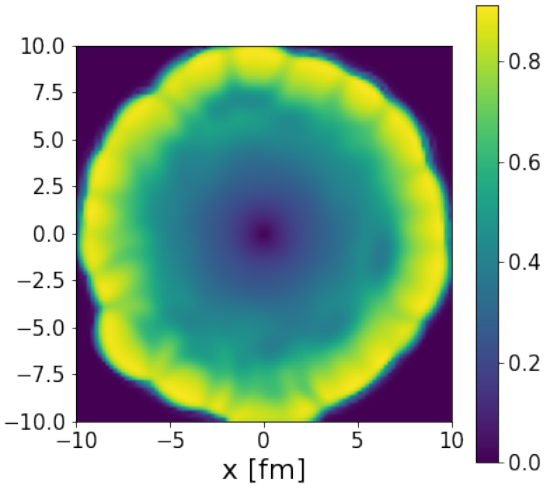

(d) fluid velocity $\overline{v_r}$ $60-61\%$

Figure 14: Background fields at the time $\tau_s = 1\text{fm/c}$ from free-streamed T$_\text{R}$ENTo initial conditions. On the left side central collisions ($0-1\%$ centrality class), on the right side peripheral collisions ($60-61\%$ centrality class) are shown. The fluid velocities are given in natural units. The energy densities are given in GeV fm^{-3}

Observing the border of the fluid velocity in Fig. 14 fluctuations can be seen. This effect, however, can be explained, by numerical inaccuracies. Even though the background is composed of 10 000 events, the resulting background field is not perfectly invariant under rotations. Underlining that those fluctuations do not have a significant impact on dynamics is the fact that the spatial position of those fluctuations on the transverse plane

is far enough away from the center. The energy densities, and thus the parton density at that position, that is associated with the fluctuations is very low. In a later section (4.2) this will be further investigated.
In the next section, the event-averaged energy and total entropy of the background fields will again be compared to "true" event-averaged total energy and total entropy considered in event-by-event simulations.

3.2.2 Determining total energy and entropy from free-streamed initial conditions

As was done in section 3.1.1, again the total entropy and the total energy are computed from the stress energy tensors using the equations (23) and (24).

Single event

Considering a time-like hyper surface $d\Sigma_\mu = (\tau_s \cdot dxdy, 0, 0)$, the total energy and entropy can be calculated by using

$$E(\tau_s) = \int\int T^{00}(\tau_s) \cdot \tau_s \cdot dxdy \quad \rightarrow \quad E(\tau_s) = \sum_{i=1}^{N}\sum_{j=1}^{N} \Delta A \cdot \tau_s \cdot T^{00}_{(i,j)}(\tau_s) \tag{42}$$

$$S(\tau_s) = \int\int s(\epsilon(\tau_s))u^0(\tau_s) \cdot \tau_s \cdot dxdy \quad \rightarrow \quad S(\tau_s) = \sum_{i=1}^{N}\sum_{j=1}^{N} \Delta A \cdot \tau_s \cdot s(\epsilon_{(i,j)}(\tau_s)) \cdot u^0_{(i,j)}(\tau_s) \tag{43}$$

Event average

For the event average it will be again differentiated between true event-average of the total energy and entropy $\langle E\rangle_{true}(\tau_s)$, $\langle S\rangle_{true}(\tau_s)$ and the total energy and entropy calculated with the background field $\langle E\rangle_{background}(\tau_s)$, $\langle S\rangle_{background}(\tau_s)$. The number of events per centrality class is N_{ev} =10 000 and N_{cen} =100 will be used.

$$\langle E\rangle_{true,\ n_{cen}}(\tau_s) = \sum_{n_{ev}=1}^{N_{ev}} \sum_{i=1}^{N} \sum_{j=1}^{N} \Delta A \cdot \tau_s \cdot T^{00}_{n_{cen},n_{ev},(i,j)}(\tau_s)/N_{ev} \tag{44}$$

$$\langle S\rangle_{true,\ n_{cen}}(\tau_s) = \sum_{n_{ev}=1}^{N_{ev}} \sum_{i=1}^{N} \sum_{j=1}^{N} \Delta A \cdot \tau_s \cdot s(\epsilon_{n_{cen},n_{ev},(i,j)}(\tau_s)) \cdot u^0_{n_{cen},n_{ev},(i,j)}(\tau_s)/N_{ev} \tag{45}$$

$$\langle E\rangle_{background,\ n_{cen}}(\tau_s) = \sum_{i=1}^{N} \sum_{j=1}^{N} \Delta A \cdot \tau_s \cdot \overline{T^{00}_{n_{cen},n_{ev},(i,j)}}(\tau_s) \tag{46}$$

$$\langle S\rangle_{background,\ n_{cen}}(\tau_s) = \sum_{i=1}^{N} \sum_{j=1}^{N} \Delta A \cdot \tau_s \cdot s(\overline{\epsilon_{n_{cen},(i,j)}}(\tau_s)) \cdot \overline{u^0_{n_{cen},(i,j)}}(\tau_s) \tag{47}$$

As a reminder: The T$_{\mathrm{R}}$ENTo initial conditions were normalized in such a way that $\langle S\rangle_{background\ 0-5\%}(\tau_s) = \langle S\rangle_{true\ 0-5\%}(\tau_s) = 11\,000 dS/dy$ to represent the correct charged particle multiplicity in both approaches.
Note, that in contrast to section 3.1.1 the total entropy is now generally not equal (compare Eq. (45) and Eq. (47)). However, when the normalization factor for the background fields is similar to the one used for the single events, then the total energy ratio $\langle E\rangle_{background}/\langle E\rangle_{true}$ will approach one. This happens, because of the inequality (41) turning into an equality. In table 1 the normalization for background fields and single events in dependence of τ_s can be found.

τ_s [fm/c]	0.1	0.3	0.5	0.7	1.0	1.5
$N_{background}/68.8$	1.7096	1.3185	1.1783	1.0979	1.0206	0.9461
$N_{true}/68.8$	1.6255	1.2539	1.1194	1.0437	0.9752	0.9140
$N_{background}/N_{true}$	0.9523	0.9510	0.9500	0.9506	0.9555	0.9661

Table 1: List of normalization factors for the background fields and the single events ("true"). The factors are divided by 68.8, which is the normalization when not considering a pre-equilibrium (see section 3.1). Additionally, the ratio of the normalization factors is given.

The normalization suggest, that the ratio $\langle E\rangle_{background}/\langle E\rangle_{true}$ will be close to one, under the assumption that small variations of the normalization will not have a great impact on the total energy.

3.2.3 The dependence of the fluctuations on free streaming time

Before total energies and total entropies will be compared, the evolution of the fluctuations of the rest frame energy ϵ is studied. The fluctuation fields of ϵ in a given centrality class n_{cen} is given as in section 3.1.2 by

$$\delta\epsilon'_{n_{cen},n_{ev},(i,j)}(\tau_s) = \frac{\epsilon'_{n_{cen},n_{ev},(i,j)}(\tau_s)}{\overline{\epsilon'_{n_{cen},(i,j)}}(\tau_s)} - 1 \quad . \tag{48}$$

The fields $\epsilon'_{n_{cen},n_{ev},(i,j)}(\tau_s)$ and $\overline{\epsilon'_{n_{cen},(i,j)}}(\tau_s)$ are calculated from $T'^{\mu\nu}_{n_{cen},n_{ev},(i,j)}(\tau_s)$. To avoid numerical complications, the fluctuation fields are only defined on the cells, where

$$\overline{\epsilon'_{n_{cen},(i,j)}}(\tau_s) \geq 0.005 \cdot \max_{i,j\in\{1,\ldots,100\}} \{\overline{\epsilon'_{n_{cen},(i,j)}}(\tau_s)\} \quad . \tag{49}$$

The indices of the cells that satisfy this condition form the index set $\mathbf{M}_{n_{cen}}(\tau_s)$.
Subsequently, the size of a fluctuation field can be defined by

$$||\delta\epsilon'_{n_{cen},n_{ev}}(\tau_s)|| := \frac{\sum_{(i,j)\in\mathbf{M}_{cen}(\tau_s)} |\delta\epsilon'_{n_{cen},n_{ev},(i,j)}(\tau_s)|\Delta A}{\#\mathbf{M}_{cen}(\tau_s)\cdot\Delta A} \quad , \tag{50}$$

where $\#\mathbf{M}_{cen}(\tau_s)$ is the size of the set $\mathbf{M}_{cen}(\tau_s)$. $\#\mathbf{M}_{cen}(\tau_s)$ accounts for the fact, that otherwise the sum would depend on the considered area.
An average of the quantity (50) is taken in two centrality classes, a central $(0-1\%)$ and a peripheral $(60-61\%)$ class. To define the average, 100 events in each class are sampled. The resulting dependence on τ_s is plotted in Fig.

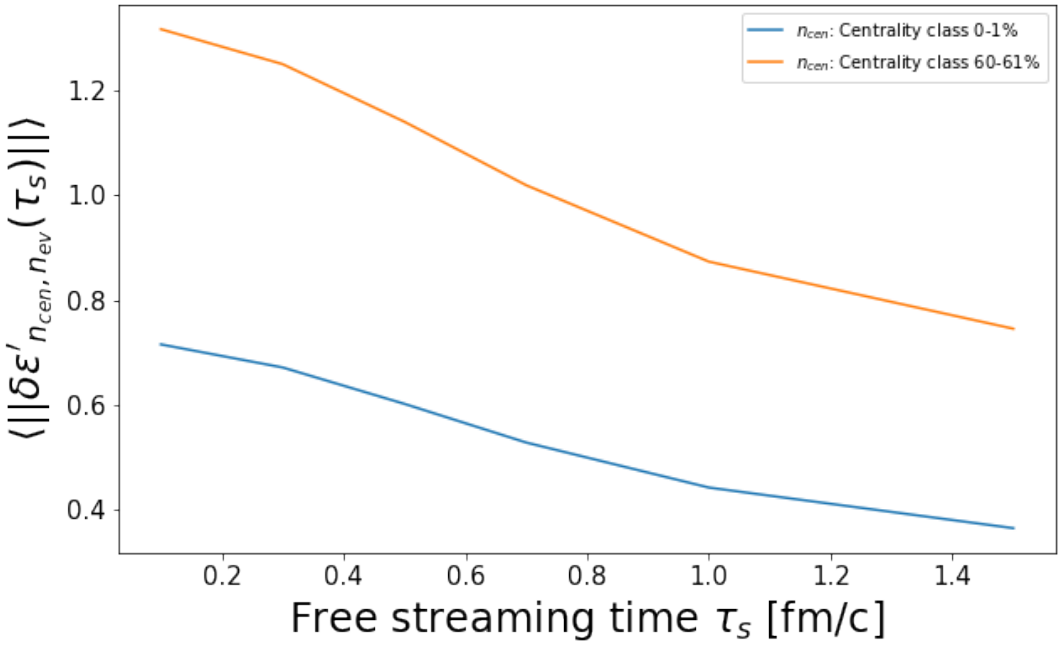

Figure 15: The size of the fluctuation field in dependence of free streaming time τ_s for a central collision $(0-1\%)$ and a peripheral collision $(60-61\%)$

Indeed, it is found that fluctuations in ϵ are reduced by the free streaming and that fluctuations for peripheral collisions are higher than central collisions. Yet, due to the fact that the landau matching procedure is not linear with respect to the fields ϵ (the landau matching can be seen as a diagonalization)

$$\bar{\epsilon} \neq \sum_{n_{ev}=1}^{N_{ev}} \epsilon_{n_{ev}} / N_{ev} \quad , \tag{51}$$

and the condition $\langle \delta\epsilon \rangle = 0$ is not satisfied anymore.

3.3 $\langle E\rangle_{background}/\langle E\rangle_{true}$ and $\langle S\rangle_{background}/\langle S\rangle_{true}$ of free streamed initial conditions

Using N_{ev} =10 000 and N_{cen} =100 the quantities $\langle E\rangle_{background}/\langle E\rangle_{true}$ and $\langle S\rangle_{background}/\langle S\rangle_{true}$ are plotted in dependence of centrality class and free streaming time τ_s (see Fig. 16).

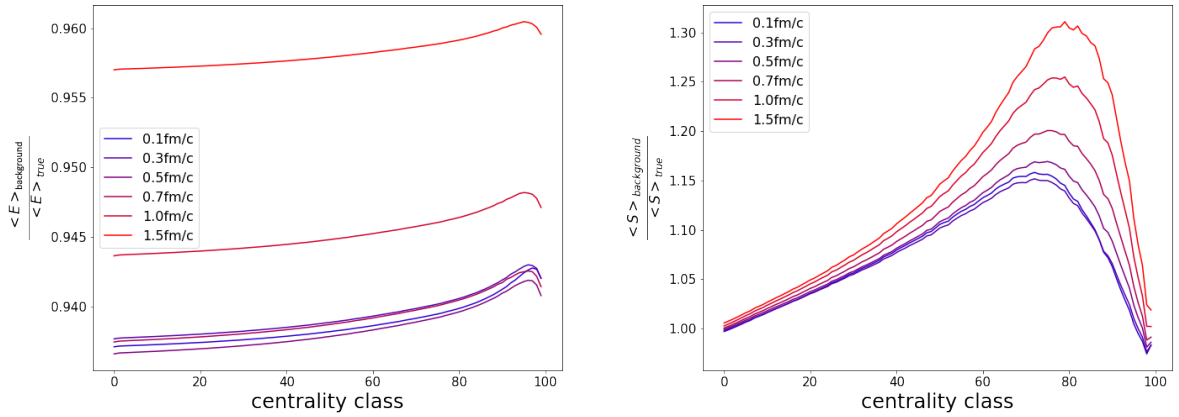

(a) Ratio of total energy $\langle E\rangle_{background}/\langle E\rangle_{true}$ **(b)** Ratio of total entropy $\langle S\rangle_{background}/\langle S\rangle_{true}$

Figure 16: Ratios of $\langle E\rangle_{background}/\langle E\rangle_{true}$ and $\langle S\rangle_{background}/\langle S\rangle_{true}$ calculated from T$_{\mathrm{R}}$ENTo initial conditions with six different free streaming times. The lines are colored from short (blue) free streaming times of $\tau_s = 0.1$fm/c to long (red) free streaming times of $\tau_s = 1.5$fm/c.

What can be seen, is that the two solution for the event averaged total energy seem to agree with each other. This is also expected, considering the statements made in the last section. Moreover, the ratio increases, especially for 1 fm/c and 1.5 fm/c, which is in agreement with the ratio of normalization factors increasing (see table 1).
For less central collisions, the ratio $\langle E\rangle_{background}/\langle E\rangle_{true}$ also increases. This can yet not fully be explained, but could be attributed to the equation of states, due to the fact that in peripheral collisions less energy and entropy density is involved. A different value of initial entropy density could have influence on how strongly the normalization effects the initial energy density and thus the total energy density after free streaming. This is rather speculative and would need to be investigated further, if one seeks to identify the source of this effect.

The ratio of total entropy starts to deviate at peripheral collisions with more free streaming time. Although, the ratio of total entropy recovers back to 1 for highly peripheral collisions, this is not expected. Initially, the discrepancy of total energy was traced back

to the size of the fluctuations (see section 3.1.2), which in turn suggested, that by reducing those fluctuations, the background approach would become more similar to real event-by-event simulations. However, the ratio of the equations for total entropy (Eq. (45) and Eq. (47)) might not be reducible to be only dependent on the fluctuations, as previously in section 3.1.2. Due to the fact that the fluctuations are in fact decreasing (see section 3.2.3), it is reasonable to suggest further investigations, where one studies how the equations for total entropy (Eq. (45) and Eq. (47)) relate to each other. This could for example be done via simplification of the problem, by assuming ideal equations of state, by neglecting shear stress and bulk viscous pressure and if necessary by assuming small free streaming times.

An additional reason for the deviating ratio of total entropy might be that the initial condition model might not be correctly describing the initial state anymore. In [14] the distribution of total charged particle multiplicity (which can be connected to total entropy [29]) was taken as an argument for or against the initial condition. This could be studied further by for example varying the reduced thickness parameter in T$_\mathrm{R}$ENTo.

The recovery of the total entropy ratio back to 1 for very peripheral collisions, is explainable by the same effects mentioned for Fig. 11, namely the recovery of azimuthal symmetry.

3.4 Motivation to study the influence of a free-streaming pre-equilibrium phase on Fluid*u*m

As was discussed in Section 3.2, free streaming builds up fluid velocity. Generally, when the hadronization is considered, a higher fluid velocity relates to higher momentum of the hadronized particles. Therefore, a parameter in the model like the free streaming time τ_s that would correlate in some way with the hardness of the particle spectra is useful when trying to optimize the model to reproduce experimental data.
It is specifically interesting to study, what will be the impact of free streaming on the mean transverse momentum of particles.
It was evident in the latter sections, that the discrepancy of the background approach and the event-by-event approach concerning total energy and entropy increased with free streaming time, even though fluctuations were reduced by the free streaming. It is not evident yet, if the increased deviation has influence on the hydrodynamic model.

4 Influence of free-streamed initial conditions on Fluid$u$M

In this chapter, the direct impact of a free streaming pre-equilibrium evolution on the particle mean transverse momentum and particle multiplicity using the hydrodynamic simulation Fluid$u$M will be investigated. We differentiate between the most abundant particles produced in Pb-Pb collisions at $\sqrt{s_{NN}} = 2.76$ TeV, namely pions, kaons and protons. The analysis will be made using events with a free streaming time of up to $1.5 fm/c$ in a range of centrality classes spanning from $0-5\%$ to $60-70\%$. The procedure to attain the initial conditions and their different implementations into the framework of Fluid$u$M will be compared with each other.

4.1 Producing initial conditions for the background and extracting radial profiles

T$_{\mathrm{R}}$ENTo version 2.0 is used with its default parameters [32] to produce 10^6 Pb-Pb events. The latter are sorted according to their produced entropy and divided into one hundred 1%-bin centrality classes. The normalized fields for the entropy density are created in the same manner as described in section 3.1. Note that the normalization factor is not dependent on centrality class and in the case of Pb-Pb with $\sqrt{s_{NN}} = 2.76$ TeV is set to 68.8 in order to retrieve the correct charged particle multiplicity. Fields for the energy density are obtained from the entropy profiles through the Equation of State (Eq. (2)). All energy density profiles are then free-streamed up to a given time τ_s, that subsequently is used in Fluid$u$M as the thermalization time, which is the starting time for the hydro evolution (the thermalization time is called τ_t, thus $\tau_t = \tau_s$). An average of the resulting stress-energy tensor fields in each centrality class is calculated. In a centrality class, the resulting tensor field defines the background field. The Landau matching procedure is used to obtain the fields $\epsilon(\tau_s)$ and $v_r(\tau_s)$ for every centrality class. In a given class, these fields describe the fluid at the thermalization time τ_s.
A flow chart as an overview for this procedure is given in Fig.17.

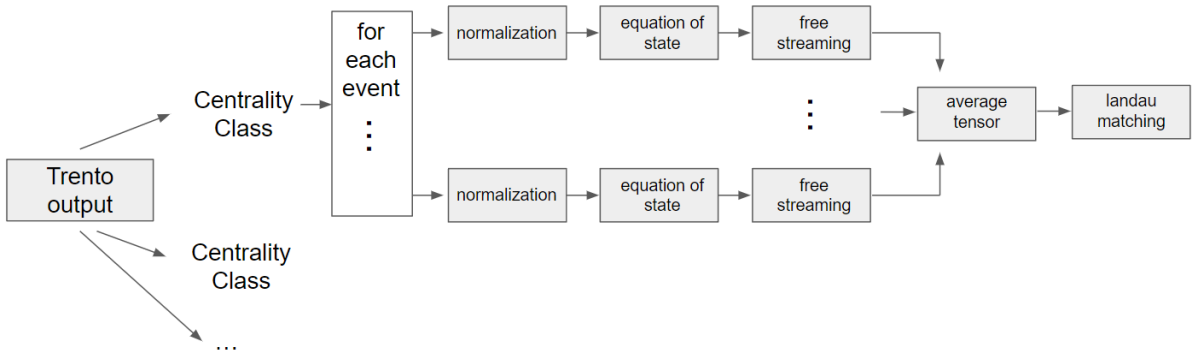

Figure 17: Procedure to compute free-streamed event-averaged initial conditions for Fluid$u$M using T$_{\mathrm{R}}$ENTo as an initial condition model.

The resulting fields for $\epsilon(\tau_s)$ and $v_r(\tau_s)$ have already been shown in a previous section (section 3.2). Fluid$u$M exploits the radial symmetry of the event-averaged initial conditions. Therefore, it is only required to provide the radial profile of the $\epsilon(\tau_s)$ and $v_r(\tau_s)$ field (see Fig.18).

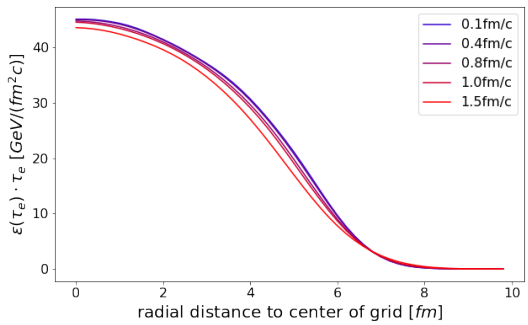

(a) energy density 0-1%

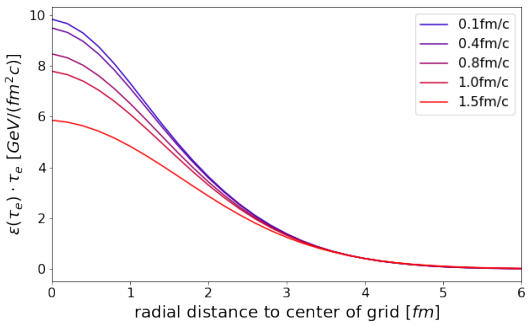

(b) energy density 60-61%

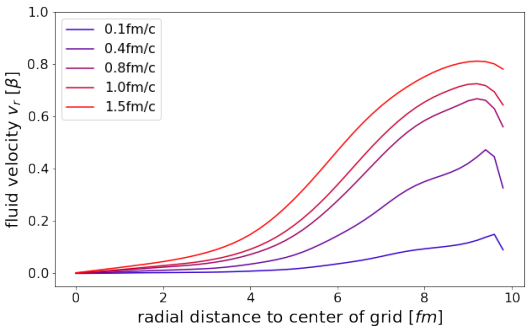

(c) fluid velocity 0-1%

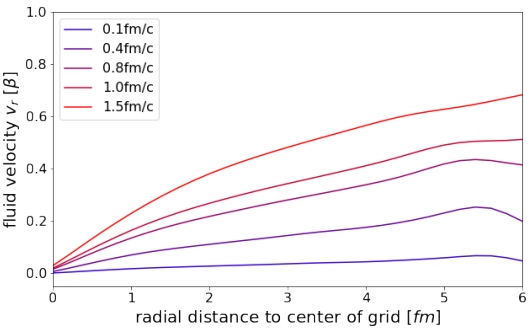

(d) fluid velocity 60-61%

Figure 18: Radial profiles of the energy density in the local fluid rest frame $\epsilon(\tau_s)$ and the radial fluid velocity v_r. The energy densities are in this plot multiplied with a factor of τ_s to make them comparable (otherwise they would decrease fast with free streaming time due to the Bjorken-expansion in longitudinal direction).

To account for the longitudinal flow of the fireball, the stress-energy tensors are being scaled with a factor of $1/\tau_s$ [19]. The scaling does not change the eigenvectors (fluid velocities u^μ) and only affects the eigenvalues (energy densities *epsilon*) of the stress-energy tensor:
In fact, letting u^μ be the time-like eigenvector of T^ν_μ with the eigenvalue $\epsilon(\tau_s)$, the eigenequation for u^μ is satisfied

$$(T^\nu_\mu/\tau_s) \cdot u^\mu = (\epsilon(\tau_s)/\tau_s) \cdot u^\nu \qquad \tau_s \in \mathbb{R} \setminus \{0\} \tag{52}$$

and thus the landau condition (see section 2.4).

4.2 Extrapolation of the profiles to the desired grid size

Fluid$u$M works with a larger transversal system size, as was used so far in the analysis. For the simulation of the initial nuclei collision and the pre-equilibrium evolution, the dynamics could be captured in an area of 20fm $\times$20fm, while the hydrodynamic phase must allow for a significant expansion of the fireball. Thus, an area of $100 \cdot \pi$ fm^2 will be considered in the simulation to prevent overflow (when the fields propagate out of the space which is captured by the grid). This requires an extrapolation of the radial profiles on hand to a range of up to 50fm.
The extrapolation of the energy density is carried out with an exponential function $e^{-r/R}$. The extrapolation of the u_r profile is done by implementing a constant tail at large r. Generally it is expected that the fluid velocity at high radial distance can't have significant impact due to the fact that in this region their respective energy densities are negligible. Therefore the outcome of the simulation should not depend on the method of extrapolation. To validate this assumption, different extrapolations were investigated.

The following extrapolations for $r > 10fm$ were examined:

$$a) \quad v_r(r) = c \quad : c = v_r(10fm) \quad b) \quad v_r(r) = a \cdot e^{-b \cdot r} \quad : a, b \in \mathbb{R}_+ \quad c) \quad v_r(r) = 0 \tag{53}$$

Those extrapolations describe; a) A constant tail, b) an exponential decreasing tail and c) a constant zero tail. Here, the extrapolation b) was fitted to cover the last two data points of the grid. In some cases this resulted in a parameter $b < 0$, due to fluctuations of v_r at large r, which then was corrected by taking the absolute value in order to maintain an exponential drop.

The total charged particle mean transverse momentum was extracted from simulations

τ_s	0.8fm/c	η/s	0.2	ζ/s	0.032
$\tilde{N}$	1.23	T_{kin}	0.14GeV	p_T	[0.1,3]GeV

Table 2: List of parameters for determination of the impact of different extrapolation methods for the fluid velocity at large radii.

done with Fluid*u*m with the set of parameters given in Table 2. The normalization factor $\tilde{N}$ was chosen such that the total multiplicity of charged particles in the centrality $0-5\%$ matches the one in experimental data[33].

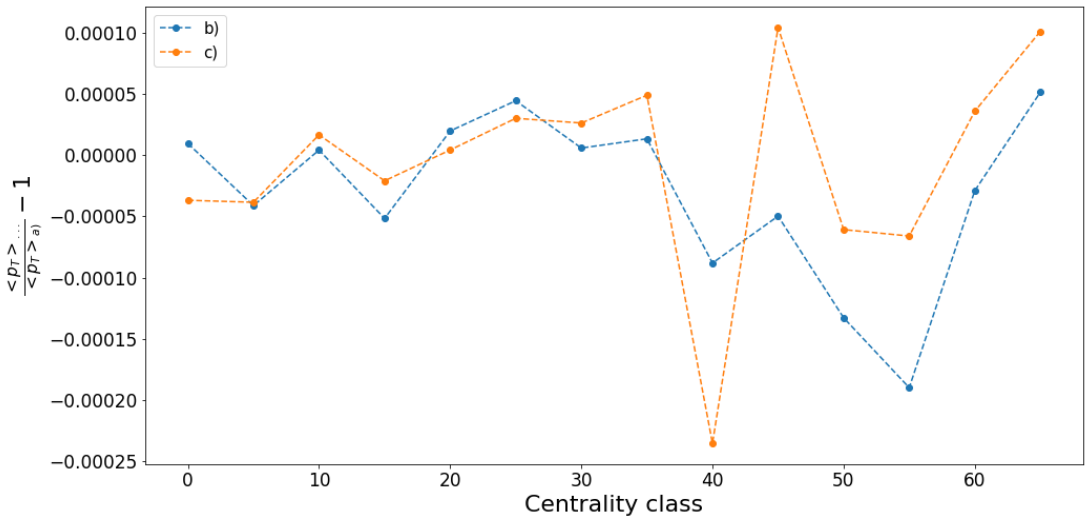

Figure 19: Comparing extrapolation models: the cases b) and c) are shown with respect to a), in different centrality classes up to $65-70\%$. The comparison is given in the ratio of $\langle p_T \rangle$ to $\langle p_T \rangle_{a)}$ minus one, and therefore represents the deviation of *b*) or *c*) to *a*).

The different results for the total $\langle p_T \rangle$ coming from extrapolation methods *b*) and *c*) were compared to *a*) in dependence of centrality class (see Fig.19). As we see, different methods give a difference of the order of $0.05-0.25\%$.

Considering that data given for this measurement has far greater relative uncertainties roughly in the range of $2-4\%$ [33], it can be verified that indeed the choice of extrapolation method will not affect the simulation in a significant way.

4.3 Impact on the calculation of $\langle p_T \rangle$ of the considered p_T range

In a analytical form, the mean transverse momentum is determined as

$$\int_0^\infty dp_T \; p_T \frac{dN}{dp_T N_{tot}} \quad .$$

Effectively, the integral is carried out with a momentum cutoff at p_{cut-} and p_{cut+} such that

$$\langle p_T \rangle = \int_{p_{cut-}}^{p_{cut+}} dp_T \; p_T \frac{dN}{dp_T N_{tot}} \quad .$$

The choice of the p_T cutoff should not impact significantly on the $\langle p_T \rangle$ itself. Another set of calculations of the total mean p_T dependent on centrality class has been carried out with the parameters given in Table 3

τ_s	0.8fm/c	η/s	0.2	ζ/s	0.032
$\tilde{N}$	1.23	T_{kin}	0.14GeV		

Table 3: List of parameters used to study the impact of the p_T range on the $\langle p_T \rangle$ observable.

A variation of the upper p_T limit from 3.0 GeV/c downward to 2.5 GeV/c and upward to 3.7 GeV/c was studied. For the lower p_T limit 0.1 GeV/c was used. The p_T range $[0.1, 3]$ GeV/c is compared to the ranges $[0.1, 3.7]$ GeV/c and $[0.1, 2.5]$ GeV/c (see Fig. 20). In experiments the range of measured p_T is dependent on the particle species with pions in a range of $[0.1, 3] GeV$, kaons in a range of $[0.2, 3] GeV$ and protons in a range of $[0.3, 4.5]$ [33].

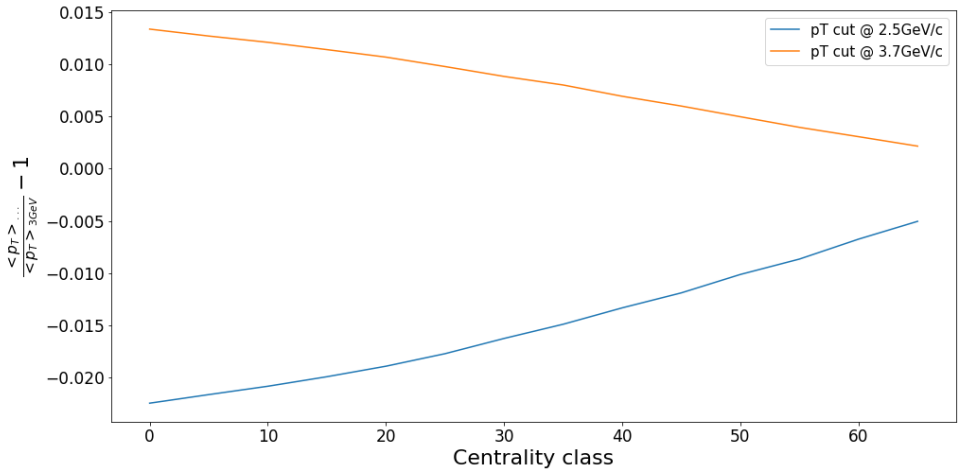

Figure 20: Comparing the simulation of $\langle p_T \rangle$ using $p_T \in [0.1, 3]$ to $p_T \in [0.1, 2.5]$ and $p_T \in [0.1, 3.7]$ in different centrality classes up to $65 - 70\%$. The comparison is given in the ratio of $\langle p_T \rangle$ to $\langle p_T \rangle_{[0.1,3]}$ minus one and therefore represents the deviation.

One can see in Fig. 20, that the relative deviation of the $\langle p_T \rangle$ observable is the strongest at high centrality, with relative deviations up to 2%. This deviation is in the same order of magnitude with the relative uncertainties of $2-4\%$ [33]. This should be kept in mind when simulating the mean particle transverse momenta. One could think that more physics is captured when a broader range of p_T is considered. However, the cut-off point of the transverse momentum can not be chosen arbitrarily high, because the hydrodynamic model gets more and more inaccurate for $p_T > 3GeV$. Partons with higher momentum (that are needed to form high momentum hadrons) can at some point not contribute to the plasma anymore, due to their shrinking cross-section. Therefore, a simulated p_T range from $0.1GeV$ to $3GeV$ will be used for the calculation of the spectra.

4.4 Calculation with Fluid$u$M using free-streamed initial conditions

In order to compare particle multiplicity and $\langle p_T \rangle$, computed for different thermalization times τ_s using accordingly long free-streamed background fields, the normalization factors $\tilde{N}$ for each thermalization time τ_s need to be determined. The normalization factors are again obtained by comparing the simulated total multiplicity for the centrality class $0-5\%$ to the experimentally determined multiplicity[33] with subsequent variation of $\tilde{N}$ until the simulation yields the correct value (see Table 4).

τ_s [fm/c]	0.1	0.4	0.8	1	1.5
$\tilde{N}$	1.184	1.18	1.116	1.09	1.06

η/s	0.2	ζ/s	0.032
T_{kin}	0.156GeV	p_T	[0.1,3]GeV

Table 4: List of parameters used for the calculation of spectra with Fluid$u$M. On the left side the normalization factors in dependance of the thermalization time, on the right side the other simulation parameters.

The same parameters as in Table 4 (right side) were used for a Fluid$u$M simulation that considered no pre-equilibrium evolution. The latter was computed with $\tau_0 = 0.4fm/c$ and $\tilde{N} = 64$. Note that the normalization in Table 4 is used in addition to the normalization used in section 4.1 with a factor of 68.8.
The result for the charged particle multiplicity density for all charged particles can be seen in Fig.21.

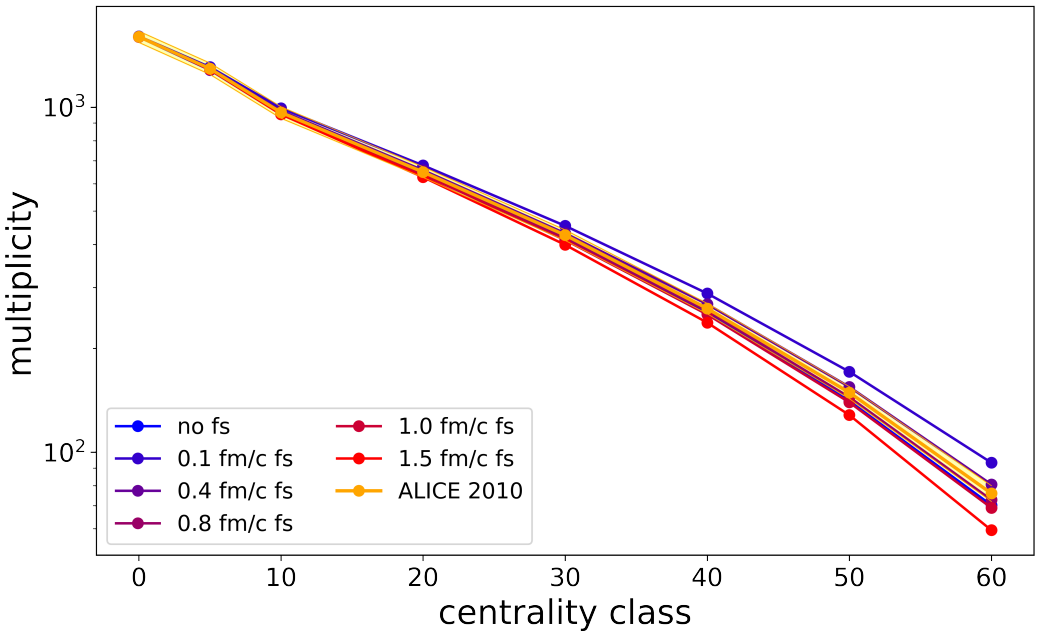

Figure 21: The figure shows the yield of multiplicity density of all charged particles at mid-rapidity $dN_{ch}/d\eta|$ simulated with and without a free streaming pre-equilibrium evolution in Fluid$u$M, in dependence of centrality class and free streaming time along with ALICE data [33]. The line describing the results without a free streaming pre-equilibrium was calculated with a thermalization time of 0.4fm/c

As can be seen the deviation between data and simulation increases with centrality class for very low and very high free-streaming times. The best agreement for the total multiplicity density is given with a free-streaming time between $0.4fm/c$ and $0.8fm/c$.

The experimental data in [33] was given in dN_π/dy, dN_K/dy and dN_p/dy at mid-rapidity. Those values were converted into $dN_\pi/d\eta$, $dN_K/d\eta$ and $dN_p/d\eta$, exploiting that at mid-rapidity $(dN_{ch}/dy)/(dN_{ch}/d\eta) \approx 1.15$ [35]. The resulting multiplicity densities of the Fluid$u$M simulation with and without free streaming, as well as the measured multiplicity densities $dN_\pi/d\eta$, $dN_K/d\eta$ and $dN_p/d\eta$ are shown in Fig.22.

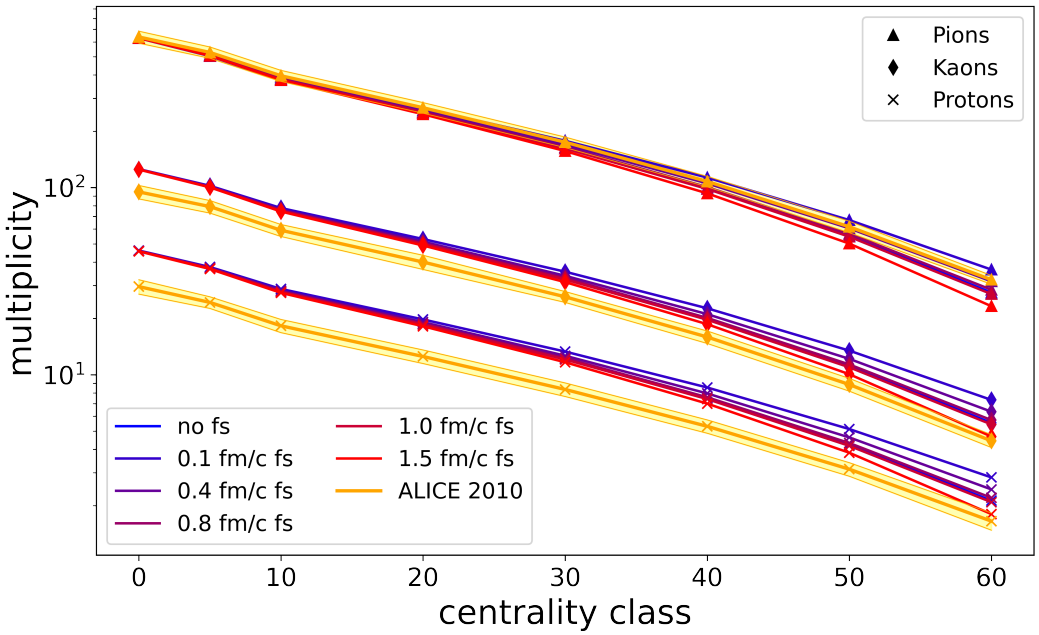

Figure 22: Multiplicity density of π, K and p simulated with and without a free streaming pre-equilibrium evolution in Fluid$u$M in dependence of centrality class along with ALICE data.

Observing the specific multiplicities of the different particles, it can be seen that using no free streaming (deep blue line) overlaps with free-streaming lines at $0.4fm/c$ to $0.8fm/c$. Multiplicity densities for kaons and protons are overestimated, which also occurs without a free-streaming phase and can be explained with an underestimation of soft pions (see Fig. 23). Due to the fact that the pions make up most of the charged particle multiplicity density, the variation of N leads to a good agreement of the simulations to pions, but resulted in an overestimation of kaons and protons.

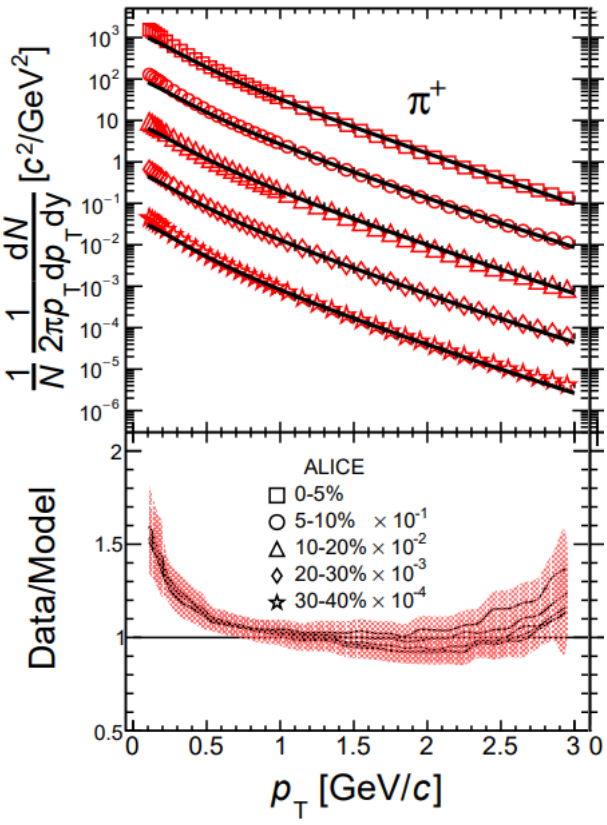

Figure 23: Spectra for pions calculated with Fluid$u$M + FastReso compared to ALICE data (Fig. from [24])

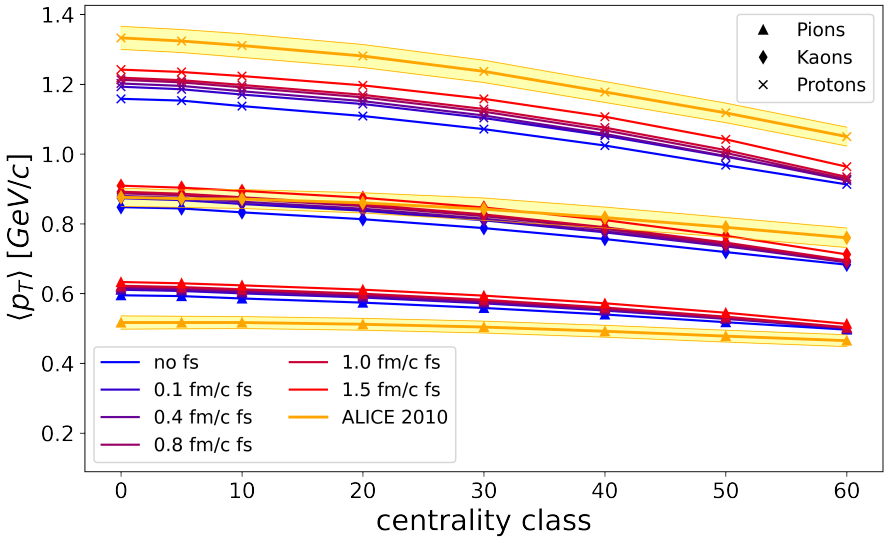

Figure 24: $\langle p_T \rangle$ of π, K and p simulated with and without a free streaming pre-equilibrium evolution in Fluid$u$M in dependence of centrality class compared to ALICE data.

The momentum spectra for pions, kaons and protons were extracted from the simulation and subsequently the mean particle transverse momentum for each species was calculated (see Fig.24). Using those values, the total mean transverse momentum for π, K and p can be determined:

$$\langle p_T \rangle_{\pi,K,P}(i_{cen}) \approx \frac{dN_\pi/d\eta \cdot \langle p_T \rangle_\pi + dN_K/d\eta \cdot \langle p_T \rangle_K + dN_P/d\eta \cdot \langle p_T \rangle_P}{dN_\pi/d\eta + dN_K/d\eta + dN_P/d\eta}(i_{cen}) \tag{54}$$

for each centrality class i_{cen}. The same was done for the experimental data. The total $\langle p_T \rangle_{\pi,K,P}$ can be seen in Fig.25. An overestimation of the pions $\langle p_T \rangle$ can be seen in Fig. 24 which worsens with increasing free streaming time. This however can also be explained with the underestimation of soft pions (Fig. 23). When considering fewer soft pions in the calculation of $\langle p_T \rangle$, the value of $\langle p_T \rangle$ is effectively increased.
The kaons can be described well by the model, especially for lower centrality classes and for free-streaming times of about $0.4fm/c - 0.8fm/c$.
Protons were underestimated before implementation of free streaming. This underestimation is still present with a free streaming evolution implemented, however the deviation decreased by about 1.5σ for central collisions.

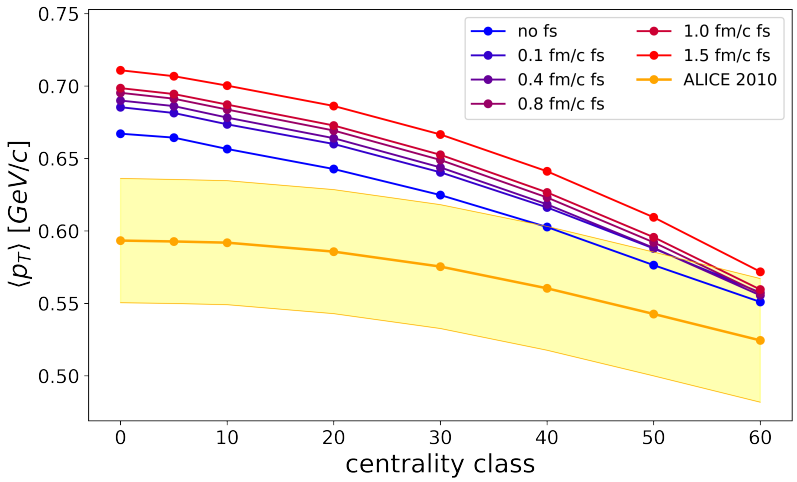

Figure 25: Total $\langle p_T \rangle_{\pi,K,P}$ simulated with and without a free streaming pre-equilibrium evolution in Fluid$u$M in dependence of centrality class along with ALICE data.

In Fig. 25 the contribution of pions to the total mean transverse momentum is very high because of their relative abundance. The $\langle p_T \rangle_{\pi,K,P}$ is therefore strongly influenced by the underestimation of soft pions. An investigation of $\langle p_T \rangle_{K,P}$ (excluding the contribution of pions) is carried out (see Fig. 26)

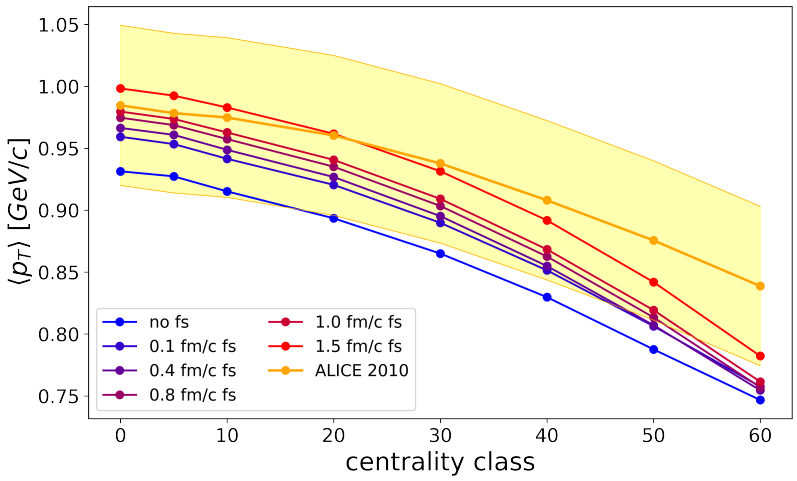

Figure 26: Total $\langle p_T \rangle_{K,P}$ simulated with and without a free streaming pre-equilibrium evolution in Fluid$u$M in dependence of centrality class along with ALICE data.

Here a slight improvement of the match between simulation and experimental data can be seen with increasing free-streaming time for central collisions. This would suggest, that an introduction of an initial fluid velocity raises the prediction for the mean transverse momentum and improves the applicability of the model, at least for low impact parameters. However, a potential problem could be, that the slope of mean transverse momentum.
For peripheral collisions, the free streaming doesn't affect $\langle p_T \rangle$ as strongly as in the central collisions.
When looking at Fig. 24, 25 and 26 the slope of the curves increases for increasing free-streaming time and decreasing centrality. This can not be found in the experimental data which shows a significantly slower reduction of measured $\langle p_T \rangle$ for peripheral collisions. A possible explanation for this effect could be, that peripheral collisions tend to have a higher initial fluid velocity, but also a lower temperature (see Fig. 18). The lowering of the temperature during free streaming occurs faster for peripheral collisions. This in turn could lead to a reduction in evolution time in the hydro phase, which might subsequently shorten the time, where further fluid velocity can be developed and therefore explain the steepening drop at lower centrality. This effect would need to be extensively studied in order to shed light on the behavior of $\langle p_T \rangle$ in peripheral collisions. Additionally, it is not clear yet, if the findings in section 3.3, where a discrepancy between the background approach and the event-by-event approach was seen, can be connected to the steepening drop at peripheral collisions, which also suggests further investigation.

5 Conclusion and Outlook

In this thesis, a pre-equilibrium free streaming phase in conjunction with a background-fluctuation splitting approach was studied. The effects of this pre-equilibrium phase on the initial condition were investigated in dependence of collision centrality and thermalization time by comparing properties of the evolved initial conditions between background field approximation and proper event-by-event simulation. Further, the effect of free streaming on a hydrodynamic simulation called Fluid$u$M using only a background field was observed and its results for particle mean multiplicity and particle mean transverse momentum were compared to experimental data from ALICE for pions, kaons and protons. No optimization of the model in terms of fitting was done yet, rather qualitative effects were studied.
In the study of the initial conditions, it was found that the discrepancy between the inspected values of total energy and total entropy did all together not improve with free streaming time. Definite results can not be formed as long as the problem is not studied more deeply. Even though, fluctuations of the fields for energy density and entropy density were reduced, the deviations of total entropy between the background approach and the event-by-event approach increased. Moreover, it is not clear if this is a phenomenon that can also be found analytically, as in section 3.1.2.
Moreover, in this study, the initial condition created with T$_\mathrm{R}$ENTo were interpreted as fields of entropy density. Another approach, treating the output of T$_\mathrm{R}$ENTo as energy densities, would simplify the procedure at hand and also might clarify what gives rise to possible deviations between the event-by-event and the background-fluctuation splitting approach after free streaming.
Furthermore, the deviations might be attributed to an inaccurate description of the initial condition, which could be investigated by observing the impact of the reduced thickness parameter in T$_\mathrm{R}$ENTo on the ratio of total entropy.

In the examination of the influence of free streaming on the model Fluid$u$M, a rise in mean transverse particle momentum with growing free streaming time can be observed. For kaons and protons, the free streaming tends to increase $\langle p_T \rangle$ for the model parameters we chose. The effect on $\langle p_T \rangle$ decreases with decreasing centrality of the collision. This behavior still needs to be investigated further. More research is necessary in order to connect the effects of free streaming on the initial conditions to the change in the dynamics of the hydrodynamic phase. For example, the evolution of the temperature profiles in the hydrodynamic phase in dependence of free streaming time can be studied. Moreover, it could be investigated, if the pre-equilibrium model decreases the evolution time of the hy-

drodynamic phase in a manner that could effectively lower mean transverse momentum. Finally, it can be summarized that implementing a free streaming pre-equilibrium provides a parameter with influence on particle mean transverse momenta and therefore enables Fluid$u$M to a potentially better description of experimental data. Implementing this parameter in grid search might verify this assumption.

List of Tables

List of Figures

References

[1] Anton Andronic et al. “Decoding the phase structure of QCD via particle production at high energy”. In: *Nature* 561.7723 (Sept. 2018), pp. 321–330. DOI: 10.1038/s41586-018-0491-6. URL: https://doi.org/10.1038%2Fs41586-018-0491-6.

[2] Alexander M. Polyakov. “Thermal Properties of Gauge Fields and Quark Liberation”. In: *Phys. Lett. B* 72 (1978), pp. 477–480. DOI: 10.1016/0370-2693(78)90737-2.

[3] Ulrich W. Heinz and Maurice Jacob. “Evidence for a new state of matter: An Assessment of the results from the CERN lead beam program”. In: (Jan. 2000). arXiv: nucl-th/0002042.

[4] the free encyclopedia Wikipedia. *Standard Model of Elementary Particles*. [Online; accessed May 24, 2023]. 2023. URL: https://en.wikipedia.org/wiki/File:Standard_Model_of_Elementary_Particles.svg.

[5] Mark Thomson. *Modern particle physics*. New York: Cambridge University Press, 2013. ISBN: 978-1-107-03426-6. DOI: 10.1017/CBO9781139525367.

[6] John B. Kogut and Leonard Susskind. "Hamiltonian Formulation of Wilson's Lattice Gauge Theories". In: *Phys. Rev. D* 11 (1975), pp. 395–408. DOI: 10.1103/PhysRevD.11.395.

[7] Brett Teeple. "Deconfinement and duality on toroidially compactified spacetimes for all gauge groups". In: (Apr. 2015), pp. -. DOI: 10.13140/RG.2.1.4716.4960.

[8] A. Bazavov et al. "Equation of state in (2+1)-flavor QCD". In: *Physical Review D* 90.9 (Nov. 2014). DOI: 10.1103/physrevd.90.094503. URL: https://doi.org/10.1103%2Fphysrevd.90.094503.

[9] I. C. Arsene et al. "Nuclear stopping and rapidity loss in Au+Au collisions at s(NN)**(1/2) = 62.4-GeV". In: *Phys. Lett. B* 677 (2009), pp. 267–271. DOI: 10.1016/j.physletb.2009.05.049. arXiv: 0901.0872 [nucl-ex].

[10] Wojciech Broniowski et al. "Free-streaming approximation in early dynamics of relativistic heavy-ion collisions". In: *Phys. Rev. C* 80 (2009), p. 034902. DOI: 10.1103/PhysRevC.80.034902. arXiv: 0812.3393 [nucl-th].

[11] Kjeld Aamodt et al. "Elliptic Flow of Charged Particles in Pb-Pb Collisions at root s(NN)=2.76 TeV". In: *Physical review letters* 105 (Dec. 2010), p. 252302. DOI: 10.1103/PhysRevLett.105.252302.

[12] Michael L. Miller et al. "Glauber modeling in high energy nuclear collisions". In: *Ann. Rev. Nucl. Part. Sci.* 57 (2007), pp. 205–243. DOI: 10.1146/annurev.nucl.57.090506.123020. arXiv: nucl-ex/0701025.

[13] Bjoern Schenke, Prithwish Tribedy, and Raju Venugopalan. "Fluctuating Glasma initial conditions and flow in heavy ion collisions". In: *Phys. Rev. Lett.* 108 (2012), p. 252301. DOI: 10.1103/PhysRevLett.108.252301. arXiv: 1202.6646 [nucl-th].

[14] Jia Liu, Chun Shen, and Ulrich W. Heinz. *Pre-equilibrium evolution effects on heavy-ion collision observables*. 2015. DOI: 10.48550/ARXIV.1504.02160. URL: https://arxiv.org/abs/1504.02160.

[15] Fred Cooper and Graham Frye. "Single-particle distribution in the hydrodynamic and statistical thermodynamic models of multiparticle production". In: *Phys. Rev. D* 10 (1 July 1974), pp. 186–189. DOI: 10.1103/PhysRevD.10.186. URL: https://link.aps.org/doi/10.1103/PhysRevD.10.186.

[16] M. Cheng et al. "The QCD equation of state with almost physical quark masses". In: *Phys. Rev. D* 77 (2008), p. 014511. DOI: 10.1103/PhysRevD.77.014511. arXiv: 0710.0354 [hep-lat].

[17] J. Scott Moreland, Jonah E. Bernhard, and Steffen A. Bass. "Alternative ansatz to wounded nucleon and binary collision scaling in high-energy nuclear collisions". In: *Phys. Rev. C* 92.1 (2015), p. 011901. DOI: 10.1103/PhysRevC.92.011901. arXiv: 1412.4708 [nucl-th].

[18] Duke-QCD. *TRENTo repository*. [Online; accessed June 9th, 2023]. 2023. URL: https://github.com/Duke-QCD/trento.

[19] J. D. Bjorken. "Highly Relativistic Nucleus-Nucleus Collisions: The Central Rapidity Region". In: *Phys. Rev. D* 27 (1983), pp. 140–151. DOI: 10.1103/PhysRevD.27.140.

[20] Duke-QCD. *freestream repository*. [Online; accessed June 9th, 2023]. 2023. URL: https://github.com/Duke-QCD/freestream.

[21] Akihiko Monnai. "Landau and Eckart frames for relativistic fluids in nuclear collisions". In: *Phys. Rev. C* 100 (1 July 2019), p. 014901. DOI: 10.1103/PhysRevC.100.014901. URL: https://link.aps.org/doi/10.1103/PhysRevC.100.014901.

[22] Stefan Floerchinger, Eduardo Grossi, and Jorrit Lion. "Fluid dynamics of heavy ion collisions with mode expansion". In: *Phys. Rev. C* 100 (1 July 2019), p. 014905. DOI: 10.1103/PhysRevC.100.014905. URL: https://link.aps.org/doi/10.1103/PhysRevC.100.014905.

[23] Aleksas Mazeliauskas et al. "Fast resonance decays in nuclear collisions". In: *Nucl. Phys. A* 1005 (2021). Ed. by Feng Liu et al., p. 121988. DOI: 10.1016/j.nuclphysa.2020.121988.

[24] D. Devetak et al. "Global fluid fits to identified particle transverse momentum spectra from heavy-ion collisions at the Large Hadron Collider". In: *Journal of High Energy Physics* 2020.6 (June 2020). DOI: 10.1007/jhep06(2020)044. URL: https://link.springer.com/article/10.1007/JHEP06(2020)044.

[25] Ulrich Heinz. ""RHIC serves the perfect fluid" – Hydrodynamic flow of the QGP". In: (Jan. 2006).

[26] P. K. Kovtun, D. T. Son, and A. O. Starinets. "Viscosity in Strongly Interacting Quantum Field Theories from Black Hole Physics". In: *Phys. Rev. Lett.* 94 (11 Mar. 2005), p. 111601. DOI: 10.1103/PhysRevLett.94.111601. URL: https://link.aps.org/doi/10.1103/PhysRevLett.94.111601.

[27] Fernando G. Gardim et al. "Thermodynamics of hot strong-interaction matter from ultrarelativistic nuclear collisions". In: *Nature Phys.* 16.6 (2020), pp. 615–619. DOI: 10.1038/s41567-020-0846-4. arXiv: 1908.09728 [nucl-th].

[28] Ekkard Schnedermann, Josef Sollfrank, and Ulrich W. Heinz. "Thermal phenomenology of hadrons from 200-A/GeV S+S collisions". In: *Phys. Rev. C* 48 (1993), pp. 2462–2475. DOI: 10.1103/PhysRevC.48.2462. arXiv: nucl-th/9307020.

[29] Giuliano Giacalone. "A matter of shape: seeing the deformation of atomic nuclei at high-energy colliders". PhD thesis. U. Paris-Saclay, 2020. arXiv: 2101.00168 [nucl-th].

[30] Fernando G. Gardim et al. "Effects of initial state fluctuations on the mean transverse momentum". In: *Nuclear Physics A* 1005 (2021). The 28th International Conference on Ultra-relativistic Nucleus-Nucleus Collisions: Quark Matter 2019, p. 121999. ISSN: 0375-9474. DOI: https://doi.org/10.1016/j.nuclphysa.2020.121999. URL: https://www.sciencedirect.com/science/article/pii/S0375947420303092.

[31] Giuliano Giacalone et al. "Correlation between mean transverse momentum and anisotropic flow in heavy-ion collisions". In: *Phys. Rev. C* 103.2 (2021), p. 024909. DOI: 10.1103/PhysRevC.103.024909. arXiv: 2004.01765 [nucl-th].

[32] Duke-QCD. *TRENTo documentation*. [Online; accessed June 9th, 2023]. 2023. URL: http://qcd.phy.duke.edu/trento/usage.html#physical-options.

[33] ALICE Collaboration. "Centrality dependence of *pi*, K, p production in Pb-Pb collisions at $\sqrt{s_{NN}}$=2.76 TeV". In: *Physical Review C* 88.4 (Oct. 2013). DOI: 10.1103/physrevc.88.044910. URL: https://doi.org/10.1103%2Fphysrevc.88.044910.

[34] Jean-Yves Ollitrault. "Relativistic hydrodynamics for heavy-ion collisions". In: *Eur. J. Phys.* 29 (2008), pp. 275–302. DOI: 10.1088/0143-0807/29/2/010. arXiv: 0708.2433 [nucl-th].

[35] Patrick Hanus, Klaus Reygers, and Aleksas Mazeliauskas. "Entropy production in pp and Pb-Pb collisions at energies available at the CERN Large Hadron Collider". In: *Physical Review C* 100.6 (Dec. 2019). DOI: 10.1103/physrevc.100.064903. URL: https://doi.org/10.1103%2Fphysrevc.100.064903.

Erklärung

Ich versichere, dass ich diese Arbeit selbstständig verfasst und keine anderen als die angegebenen Quellen und Hilfsmittel benutzt habe.

Heidelberg, den 09.06.2023,